Measuring the angular momentum distribution in core-collapse supernova progenitors with gravitational waves

Ernazar Abdikamalov,[1,*] Sarah Gossan,[1,†] Alexandra M. DeMaio,[2,1,‡] and Christian D. Ott[1,3,§]

[1]*TAPIR, MC 350-17, California Institute of Technology, 1200 East California Boulevard, Pasadena, California 91125, USA*

[2]*Department of Physics and Astronomy, Rutgers, The State University of New Jersey, 136 Frelinghuysen Road Piscataway, New Jersey 08854-8019, USA*

[3]*Kavli IPMU (WPI), University of Tokyo, Kashiwa 277-8583, Japan*

(Received 26 November 2013; published 1 August 2014)

The late collapse, core bounce, and the early postbounce phase of rotating core collapse leads to a characteristic gravitational wave (GW) signal. The precise shape of the signal is governed by the interplay of gravity, rotation, nuclear equation of state (EOS), and electron capture during collapse. We explore the detailed dependence of the signal on total angular momentum and its distribution in the progenitor core by means of a large set of axisymmetric general-relativistic hydrodynamics core-collapse simulations, in which we systematically vary the initial angular momentum distribution in the core. Our simulations include a microphysical finite-temperature EOS, an approximate electron capture treatment during collapse, and a neutrino leakage scheme for the postbounce evolution. Our results show that the total angular momentum of the inner core at bounce and the inner core's ratio of rotational kinetic energy to gravitational energy $T/|W|$ are both robust parameters characterizing the GW signal. We find that the precise distribution of angular momentum is relevant only for very rapidly rotating cores with $T/|W| \gtrsim 8\%$ at bounce. We construct a numerical template bank from our baseline set of simulations, and carry out additional simulations to generate trial waveforms for injection into simulated Advanced LIGO noise at a fiducial galactic distance of 10 kpc. Using matched filtering, we show that for an optimally oriented source and Gaussian noise, Advanced LIGO could measure the total angular momentum to within $\pm 20\%$, for rapidly rotating cores. For most waveforms, the nearest known degree of precollapse differential rotation is correctly inferred by both our matched filtering analysis and an alternative Bayesian model selection approach. We test our results for robustness against systematic uncertainties by injecting waveforms from simulations utilizing a different EOS and variations in the electron fraction in the inner core. The results of these tests show that these uncertainties significantly reduce the accuracy with which the total angular momentum and its precollapse distribution can be inferred from observations.

DOI: 10.1103/PhysRevD.90.044001 PACS numbers: 04.25.D-, 95.85.Sz, 97.60.Bw, 97.60.Jd

I. INTRODUCTION

Massive stars [$8M_\odot \lesssim M \lesssim 130M_\odot$, at zero age main sequence (ZAMS)] undergo collapse at the end of their nuclear burning lives once their electron-degenerate core exceeds its effective Chandrasekhar mass. The inner core collapses subsonically and, when its density exceeds that of nuclear matter, experiences core bounce due to the stiffening of the nuclear equation of state (EOS). A hydrodynamic shock forms at the interface of inner and supersonically collapsing outer core. The shock quickly moves out, but stalls within a few tens of milliseconds at a radius of 100–200 km, due to dissociation of infalling iron-group nuclei and energy losses to neutrinos that stream away from the semitransparent region behind the shock [1]. The shock must be revived by some mechanism to drive an explosion and create the spectacular display of a core-collapse supernova across the electromagnetic spectrum.

For the vast majority of core-collapse supernovae with explosion energies of ~0.1–1 B (1 B*ethe* $= 10^{51}$ erg), the neutrino mechanism [2–4] is the favored mechanism of shock revival. It relies on the deposition of a fraction of the outgoing electron neutrino and electron antineutrino luminosity (with a typical efficiency of order 10%) behind the stalled shock, but also requires neutrino-driven convection and/or the standing accretion shock instability (SASI; e.g., [5]) to increase the dwell time of accreted matter in the region behind the shock where net energy absorption is possible. The neutrino mechanism fails in spherical symmetry (one dimension, where convection and SASI are absent). A number of axisymmetric (two-dimensional) core-collapse supernova simulations with detailed energy-dependent neutrino transport and microphysics now report successful explosions [6–8], but the first such three-dimensional simulations are not yet conclusive

*abdik@tapir.caltech.edu
†sarah.gossan@tapir.caltech.edu
‡amd320@eden.rutgers.edu
§cott@tapir.caltech.edu

[9,10]. Other physics or effects such as precollapse asphericities due to vigorous convective shell burning may be needed to enable robust explosions in three dimensions [11].

There is, however, a class of highly energetic core-collapse supernovae with inferred explosion energies of up to 10 B that the neutrino mechanism alone seems too feeble to possibly explain. This class includes relativistic type Ic supernovae with strongly Doppler-broadened spectral lines from compact hydrogen/helium-poor progenitors (so-called type Ic-bl supernovae; e.g., [12,13]) and super-energetic type II supernovae from red supergiants (e.g., [14,15]) and makes up 1–2% of all core-collapse supernovae [13]. All supernovae associated with long gamma-ray bursts have been of type Ic-bl [16,17].

Such energetic events may require a central engine that can convert the gravitational energy provided by collapse much more efficiently into energy of the explosive outflow than neutrinos are capable of. One possibility is the magnetorotational mechanism in which a millisecond-period protoneutron star with magnetar-strength magnetic fields drives a jet-driven bipolar explosion [18–22], which, in some cases, might set the stage for a subsequent long gamma-ray burst (e.g., [23,24]).

Current standard lore of stellar evolution theory and pulsar birth-spin estimates states that most massive stars are rather slow rotators at the end of their lives, having lost angular momentum to stellar winds and not being strongly differentially rotating due to angular momentum redistribution by magnetic torques (e.g., [25,26]). Special conditions, such as chemically homogeneous evolution at low metallicity [27,28] or binary interactions [29], might be necessary to produce the progenitors of hyperenergetic core-collapse supernovae and long gamma-ray bursts.

This may or may not be the case. Current stellar evolutionary calculations are still one dimensional and take into account rotation and angular momentum loss and redistribution only approximately and in a parametrized, nonself-consistent way. Pulsar birth-spin estimates, which are based on magnetic-dipole radiation, could be off by large factors if early spin-down occurred by direct conversion of spin energy into magnetic field and/or kinetic energy of an explosive outflow. Keeping this in mind, it is not inconceivable that rotation could play a significant role in many core-collapse supernovae. Rotating core collapse naturally leads to differential rotation in the outer protoneutron star and in the postshock region [26,30]. The free energy in differential rotation[1] could be tapped by the magnetorotational instability (e.g., [31–33]), which could either lead to the growth of large-scale magnetic fields (via a dynamo; as argued for by [22,33]) or local dissipation (and additional heating) by reconnection [34]. Depending on precollapse spin and magnetization, both possibilities could either subdominantly assist the neutrino mechanism in reviving the shock, or dominate the dynamics in a magnetorotational [22,34,35] explosion.

Gravitational waves (GWs) are the most direct and best probes of rotation in stellar collapse and core-collapse supernovae. Rotation naturally leads to a quadrupole (i.e., oblate) deformation of the collapsing core. The centrifugally deformed core undergoes extreme accelerations during the late collapse, bounce, and early postbounce phase. This provides an extremely large accelerated quadrupole moment (e.g., [36]), resulting in a GW burst signal that, depending on the amount of angular momentum in the inner core, can be detected by the upcoming advanced generation of GW detectors out to 10–100 kpc [37–39]. After core bounce, on a timescale of tens of milliseconds, nonaxisymmetric dynamics may develop due to rotational shear instabilities (e.g., [40–44]), leading to longer-term quasiperiodic GW emission.

Much effort has gone into modeling the GW signal from rotating core collapse and bounce over the past three decades [37,38,40,45–55] and the current state of the art is set by simulations in conformally flat or full general relativity (GR) that includes realistic EOS and approximate neutrino transport [37–39,42]. These studies found that the GW signal from rapidly rotating core collapse and bounce has rather simple morphology and can be described by a prebounce rise in GW strain h, a large spike at bounce, and a subsequent postbounce ring-down phase in which the protoneutron star hydrodynamically dissipates its remaining pulsational energy from bounce. Simulations that included magnetic fields showed that the bounce and very early postbounce phase and the associated GW signal are not affected by magnetohydrodynamic effects unless the precollapse seed fields are unrealistically large ($B \gtrsim 10^{12}$) [55–59]. Dimmelmeier *et al.* [37] and Abdikamalov *et al.* [39] showed that the peak GW strain from collapse and bounce depends primarily and sensitively on the mass and angular momentum of the inner core at bounce. Dimmelmeier *et al.* [37], who considered two finite-temperature nuclear EOS, the EOS of Shen *et al.* [60,61], and the Lattimer-Swesty EOS [62], found only a weak dependence of the GW signal on the nuclear EOS. Ott *et al.* [38] recently showed that in rapidly rotating cores that produce protoneutron stars with spin periods $\lesssim 5$ ms, the GW signal depends on the angular momentum of the precollapse core, but not on its detailed structure and progenitor ZAMS mass. Furthermore, they demonstrated that postbounce neutrino emission has little influence on the GW signal from bounce and ring down.

In this work, we extend previous studies and focus on the influence of the angular momentum distribution in the

[1]At fixed total angular momentum, uniform rotation is the lowest energy state. Any process capable of redistributing angular momentum will operate on differential rotation, driving a system towards uniform rotation.

progenitor core on the GW signal of rotating core collapse, bounce, and ring down. To this end, we carry out 124 axisymmetric simulations with the GR core-collapse code CoCoNuT [39,63,64]. For collapse and the very early postbounce phase, axisymmetry is an excellent approximation (unless the inner part of the iron core contains large nonaxisymmetric perturbations, which is unlikely; cf. [40,42,53]). We employ the Lattimer-Swesty $K = 220$ MeV EOS [62] and treat electron capture during collapse with the deleptonization scheme of [37,65]. After bounce, we employ the neutrino-leakage scheme used in [38]. Motivated by the findings of [38], we consider only a single progenitor model [the 12-$M_\odot$ (at ZAMS) solar-metallicity progenitor of [66]] and carry out a systematic set of simulations with five different degrees of differential rotation and a fine-grained grid of initial central angular velocities. In order to understand systematic uncertainties in our simulations, we explore their dependence on the nuclear EOS and the electron fraction in the inner core.

The results of our simulations show that the GW signal of rapidly rotating cores has a strong and systematic dependence on the precollapse degree of differential rotation in cores that collapse to rapidly rotating protoneutron stars with ratio of rotational kinetic energy to gravitational energy $\beta = T/|W| \gtrsim 0.08$. The GW signal of more slowly spinning cores has little dependence on differential rotation and instead just depends on the core's "total rotation," parametrized by its $\beta = T/|W|$ at core bounce. We supplement our simulation results with a matched filtering analysis and a Bayesian model selection analysis motivated by [67]. Assuming Advanced LIGO (aLIGO; [68]) design sensitivity, we demonstrate that it is possible to measure total rotation (i.e., β or the angular momentum J) within ~20% for unknown injected rotating core-collapse signals from galactic events, assuming optimal source-detector orientation and Gaussian noise. We also show that the degree of differential rotation can be estimated, but robustly only for rapidly rotating models and if the EOS and inner-core electron fraction are known.

This paper is organized as follows. In Sec. II, we describe our computational code and in Sec. III we discuss our precollapse configurations. Section IV presents the results of our core-collapse simulations and analyzes the effects of differential rotation on dynamics and GW signal. In Sec. V, we present the matched filtering analysis and Bayesian model selection results. We summarize and conclude in Sec. VI.

II. METHODS

We perform our simulation in axisymmetric (two-dimensional) conformally flat GR with the CoCoNuT code, which has been extensively described in [37,39,50,64]. The conformal-flatness condition (CFC) has been shown to be an excellent approximation to full GR in the context of rotating stellar collapse to protoneutron stars, including the regime of strongly differential rotation [51,53,69] (see also Secs. VB and VIC8 of [70]). For the timescales considered in this work, the small systematic errors due to CFC approximation are completely dwarfed by the systematic uncertainties associated with the nuclear EOS and the treatment of neutrinos. CoCoNuT employs Eulerian spherical coordinates and solves the nonlinear elliptic CFC equations using spectral methods [64]. GR hydrodynamics is implemented following the Valencia formulation [71] via a finite-volume method with piecewise parabolic reconstruction [72] and the approximate HLLE Riemann solver [73]. The version of CoCoNuT used here is the same as in [39], but we have upgraded the EOS and neutrino microphysics routines as described in the following.

We use the tabulated finite-temperature nuclear EOS by Lattimer and Swesty [62] with $K = 220$ MeV generated by [74] and available for download from STELLARCOLLAPSE.ORG. More information on this EOS and the details of its implementation in a tabulated form can be found in [74,75]. In order to study the effect of the nuclear EOS itself, we repeat a select set of our models with the Shen *et al.* [60,61] EOS, a table of which is also available on STELLARCOLLAPSE.ORG.

We employ the neutrino microphysics routines provided by the open-source code GR1D [74,76], also available for download from STELLARCOLLAPSE.ORG. During the collapse phase, we use the parametrized $Y_e(\rho)$ deleptonization scheme [77] with the same parameters used in [38] (see the Appendix for details). In the postbounce phase, we use the neutrino leakage/heating scheme of [74] that approximates deleptonization, neutrino cooling, and heating. We implement the optical depth calculation along radial rays aligned with CoCoNuT's radial zones and use the default heating scaling factor $f_{\rm heat} = 1$ of this scheme. We take into account the contribution from neutrinos to the hydrodynamic pressure and the spacetime stress-energy tensor in the optically thick region via the ideal Fermi gas approximation above a fiducial neutrino trapping density of 2×10^{12} g cm^{-3}, following the prescription of [77]. This leakage/heating scheme has also been applied in the multidimensional simulations of [38,78,79].

As in previous studies (e.g., [37,39]), we perform our simulations in a spherical domain spanning 3000 km in radius under the assumption of equatorial symmetry. In our production simulations, we cover our domain with 250 logarithmically spaced radial grid points with a central resolution of 250 m. The 90° of our domain are covered with 40 equidistant angular grid points. We have performed a resolution study to ensure that this resolution is sufficient for the purpose of this study.

We carry out our simulations from the onset of collapse until 25 ms after bounce. By this time, postbounce ringdown oscillations of the protoneutron star have ebbed away

and the protoneutron star has settled into a quasistationary state. We extract GWs using the variant of the Newtonian quadrupole formula given in [64], which is very accurate in the case of rotating stellar collapse to protoneutron stars [80]. More specifically, this method has negligible phase error, while the GW strain amplitudes are captured within a few percent of their true values obtained in full GR simulations with Cauchy-characteristic extraction [80]. This level of accuracy is sufficient for studying how the waveforms depend on rotation and the degree of differential rotation, which is the main goal of this paper. The gravitational waveforms from all of our simulations are available from STELLARCOLLAPSE.ORG/GWCATALOG

III. INITIAL MODELS

Existing presupernova stellar models with rotation are evolved using spherically symmetric codes assuming shellular rotation (e.g., [25,27,81]). In these models, the key processes that determine the precollapse rotational configuration, such as the magnetic braking [e.g., [82]] and mass loss [e.g., [83]], are treated only approximately, while the potentially important effects of binary interactions [e.g., [29]] are generally not included at all.

Since our knowledge of the precollapse rotational configuration is far from being certain, we employ the nonrotating 12-$M_\odot$ solar-metallicity progenitor model of [66] (model s12WH07) and impose a simple parametrized rotation profile, which facilitates control of the total angular momentum and its distribution. We use the cylindrical rotation law of [48,52],

$$\Omega(\varpi) = \Omega_c \left[1 + \left(\frac{\varpi}{A}\right)^2\right]^{-1}, \qquad (1)$$

where Ω_c is the initial central angular velocity, ϖ is the cylindrical radius, and A is the parameter that controls the degree of differential rotation. This rotation law yields constant specific angular momentum at $\varpi \gg A$. Upon mapping into the code, the spherically symmetric initial model is set into rotation according to Eq. (1). Collapse proceeds more slowly than the sound crossing time of the core and the latter is quickly driven into an oblate shape by centrifugal effects. The validity of this approach was studied by [48].

It is important to note that it is currently unclear how realistic the rotation law given by Eq. (1) is. We use it nevertheless, since it represents the current standard way in which to set up rotating core collapse and because we require a rotation law that (i) roughly reproduces the angular momentum distribution expected in stellar cores,[2] (ii) does not violate any known physical principles and constraints that are relevant in this regime, and (iii) allows us to easily construct models with different amounts and distributions of angular momentum. The rotation law given by Eq. (1) fulfils these requirements.

We restrict our analysis to a single progenitor model, since different models with the same distribution of angular momentum as a function of enclosed mass are likely to produce very similar dynamics and GW signals at bounce and in the early postbounce ring-down phase. This was demonstrated by [38].

We consider five sets of models with five different values of the differential rotation parameter A: $A1 = 300$ km, $A2 = 417$ km, $A3 = 634$ km, $A4 = 1268$ km, $A5 = 10000$ km. Figure 1 depicts the ratio Ω/Ω_c as a function of mass coordinate for these values of A in the s12WH07 progenitor model. The higher the value of A, the weaker the differential rotation. The specific choices of Ai are motivated as follows: $A3$ is the same value used in [38] and gives an angular velocity at a mass coordinate of $1M_\odot$ that is one half of the central value. $A4$ is twice as large as $A3$, allowing us to probe somewhat more rigid initial rotation, and $A5$ ensures near uniform rotation in the inner $1.5M_\odot$ (corresponding to a radius of $\sim 3 \times 10^3$ km). $A1$ corresponds to extreme differential rotation, and $A2$ is in the middle between $A1$ and $A3$.

For each choice of A, we simulate sequences of models with initial central angular velocities starting at $\Omega_{c,\min} = 1\ \mathrm{rad\,s^{-1}}$ (for this value, rotation is dynamically insignificant in all models). We increase Ω_c in steps of $0.5\ \mathrm{rad\,s^{-1}}$. In models with weak or moderate differential rotation (sequences $A3 - A5$) the maximum initial central angular velocity $\Omega_{c,\max}$ is set by the value at which such models still

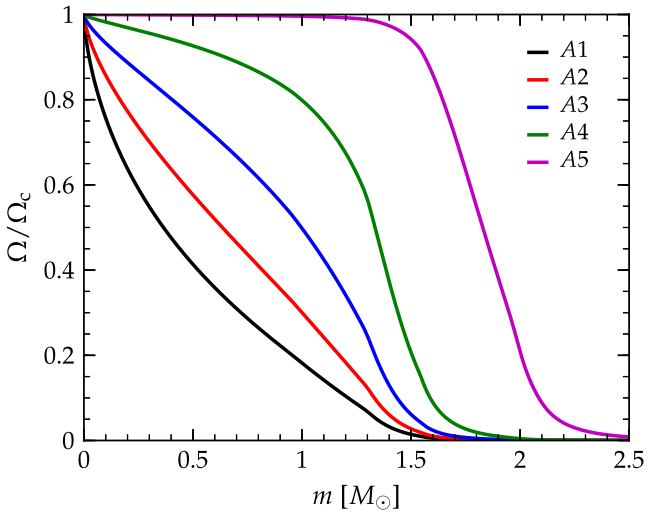

FIG. 1 (color online). The ratio of the angular velocity to the central angular velocity as a function of the enclosed-mass coordinate along the equatorial plane for the s12WH07 progenitor and for the five different values of the differential rotation parameter A considered in this study (cf. Table I).

[2]The rotation law given by Eq. (1) reproduces the radial angular momentum distribution in, e.g., rapidly rotating models 16TI and 16OM of Woosley and Heger [27] with reasonable accuracy in the inner $\sim 2M_\odot$ for $A \sim 850$ km.

collapse. For more differentially rotating models, we choose $\Omega_{c,max}$ in such a way that we obtain the global maximum of $\beta_{ic,b} = (T/|W|)_{ic,b}$, the ratio of rotational kinetic energy to gravitational energy of the inner core at bounce. We compute $T/|W|$ via the definition given by [84] and focus on the inner core, because the bounce dynamics and the associated GW signal are determined by its spin and mass [37,39]. Note that models with $\Omega_c > \Omega_{c,max}$ yield decreasing $\beta_{ic,b}$ (see, e.g., the discussions in [26,37,52]). Since such models collapse only in the case of very strong differential rotation, they are not useful for our goal of comparing different degrees of differential rotation.

IV. RESULTS: DYNAMICS AND WAVEFORMS

The top panel of Fig. 2 depicts the time evolution of the central density ρ_c during the last phase of collapse, bounce, and the early postbounce phase of model $A3O6$, which is representative for many of the simulated models. For future reference, we define the time of core bounce as the moment at which the specific entropy at the edge of the inner core in the equatorial plane reaches $3k_B$ baryon^{-1}. Just before bounce, ρ_c increases rapidly due to the accelerated contraction of the inner core. Once nuclear density is reached, the stiffening of the nuclear EOS abruptly decelerates collapse. The inner core overshoots its equilibrium configuration due to its immense inertia, and consequently ρ_c reaches $\sim 3.7 \times 10^{14}$ g cm^{-3} at maximum contraction. The core bounces back and settles at a postbounce (pb) quasiequilibrium central density $\rho_{c,pb}$ of $\sim 3 \times 10^{14}$ g cm^{-3}, after a series of ring-down oscillations that last for ~10–15 ms. These oscillations are clearly visible in the evolution of the central density in the postbounce phase as a quasiperiodic ~7% variation of ρ_c.

The middle panel of Fig. 2 shows $\beta = T/|W|$ of the inner core for model $A3O6$. By construction, β directly reflects the importance of rotational support in gravitationally bound objects [85]. β_{ic} grows in the final phase of collapse due to the spin-up of the inner core, as a consequence of angular momentum conservation. At bounce, β_{ic} peaks at ~0.1 in this model, before decreasing to ~0.08 while the inner core settles into its postbounce quasiequilibrium. The ring-down protoneutron star oscillations in the postbounce phase are also visible as small variations in β_{ic}.

In Fig. 3, we show $\beta_{ic,b}$ as a function of the initial central angular velocity Ω_c for all models. At fixed Ω_c, strongly differentially rotating models reach smaller $\beta_{ic,b}$ than more uniformly rotating ones. This is due to the comparatively modest total angular momentum in the former's inner cores. With increasing Ω_c, uniformly and mildly differentially rotating models (sequences $A3 - A5$) eventually become fully centrifugally supported at the start of the

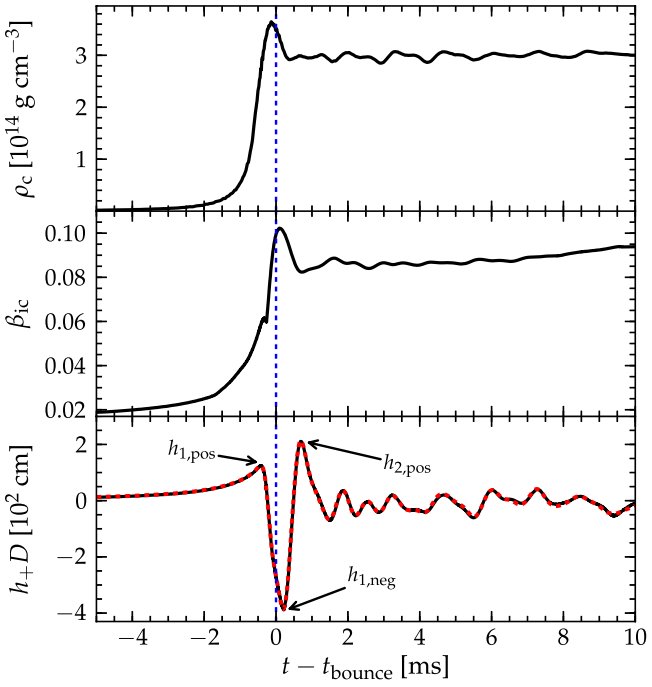

FIG. 2 (color online). Time evolution of the central density (top panel), β_{ic} (center panel), and GW strain (bottom panel; rescaled by source distance D) in model $A3O6$. The arrows indicate the first three pronounced generic features of the GW signal, labeled $h_{1,pos}$, $h_{1,neg}$, $h_{2,pos}$, and $h_{2,neg}$. The thin vertical dashed line indicates the time of core bounce defined as the time at which the equatorial edge of the inner core reaches an entropy of $3k_B$ baryon^{-1}. The dashed red line shows the GW strain for the same model simulated with 50% higher resolution in both the angular and radial direction. There is excellent agreement, which suggests that our fiducial resolution yields converged results.

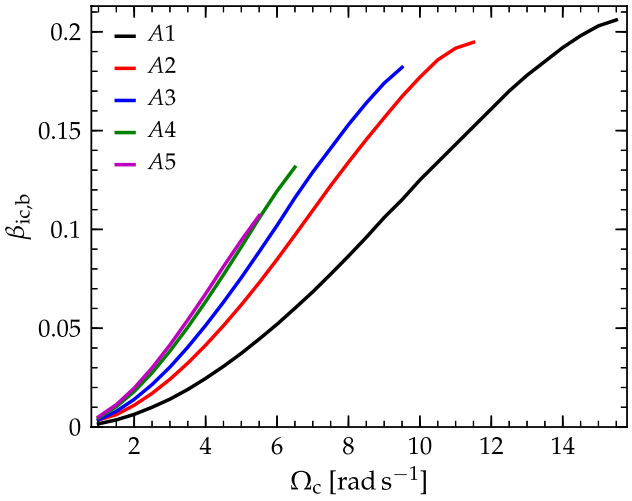

FIG. 3 (color online). Ratio of rotational kinetic energy to gravitational energy of the inner core at bounce $\beta_{ic,b}$ as a function of initial central angular velocity Ω_c. All model sequences, from near uniform rotation ($A5$) to strong differential rotation ($A1$), are shown. Sequences with uniform or moderate differential rotation terminate at Ω_c beyond which they would be fully centrifugally supported already at the onset of collapse; cf. Table I. Note that the mapping $\Omega_c \to \beta_{ic,b}$ depends on progenitor structure [38].

simulation and do not collapse. Due to this, the graphs in Fig. 3 for such models terminate at small to moderate Ω_c, and the corresponding maximum $\beta_{\rm ic,b}$ reached for sequences $A5$, $A4$, and $A3$ are 0.11, 0.13, and 0.18, respectively.

More strongly differentially rotating models, however, collapse even at high Ω_c. Sequences $A2$ and $A1$ reach $\beta_{\rm ic,b}$ of 0.19 and 0.21, respectively. The graphs corresponding to these models in Fig. 3 show that these values are very close to the obtainable global maximum. A further increase in Ω_c would lead to a decrease in $\beta_{\rm ic,b}$, because bounce occurs centrifugally at lower core densities, corresponding to a smaller degree of spin-up (see the extensive discussions in [26,39,52]).

A. Influence of differential rotation on collapse, bounce, and early postbounce dynamics

The central objective of this work is to infer the effects of the angular momentum distribution in the progenitor core on the dynamics of core collapse, bounce, the early ringdown oscillations, and the resulting GW signal. As demonstrated already in previous work (e.g., [37,54]), the effect on the inner core is most important, since its mass and angular momentum (and, perhaps, its distribution) determine the GW signal. We will discuss the details of the latter in Sec. IV B.

As a start, it is useful to define a quantity that describes the total rotation of the inner core. One possibility is to use the already introduced quantity $\beta_{\rm ic}$. It is most useful to consider the value of $\beta_{\rm ic}$ at bounce, since this is also the time at which the highest GW amplitudes occur. An obvious alternative choice is the total angular momentum of the inner core $J_{\rm ic}$, which, again, is best considered at the time of core bounce. Another alternative, though less direct, measure is the mass of the unshocked inner core at bounce $M_{\rm ic,b}$. In the nonrotating case, $M_{\rm ic,b}$ is determined by the trapped lepton fraction in the inner core (e.g., [1]). Rotation increases $M_{\rm ic,b}$ by slowing down collapse and thus allowing a greater amount of material to be in sonic contact and part of the inner core [37,39,46].

Figure 4 shows that $\beta_{\rm ic,b}$, $J_{\rm ic,b}$, and $M_{\rm ic,b}$ obey a simple linear relationship and are independent of the degree of differential rotation through most of the considered model parameter space. Thus they can be used interchangeably to describe "total rotation." The simple relationship becomes nonlinear and dependent on the differential rotation parameter A only for very rapid rotation ($\beta_{\rm ic,b} \gtrsim 0.13$, $J_{\rm ic,b} \gtrsim 6 \times 10^{48}$ erg s, $M_{\rm ic,b} \gtrsim 0.8 M_\odot$).

The mapping $\beta_{\rm ic,b} \rightarrow J_{\rm ic,b}$, shown in the lower panel of Fig. 4, exhibits interesting dependence on A in rapidly rotating models with $\beta_{\rm ic,b} \gtrsim 0.13$–$0.15$. More differentially rotating models have systematically less $J_{\rm ic,b}$ at fixed $\beta_{\rm ic,b}$ than less differentially rotating ones. This is straightforward to understand, since, at fixed $J_{\rm ic,b}$ and $M_{\rm ic,b}$, a more differentially rotating inner core will always have more

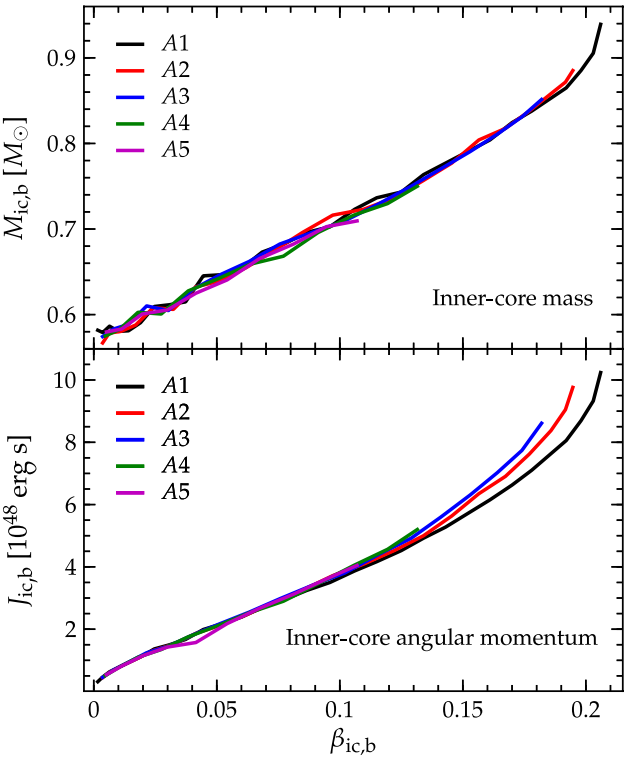

FIG. 4 (color online). Mass of the inner core at bounce ($M_{\rm ic,b}$, top panel) and angular momentum ($J_{\rm ic,b}$, bottom panel) as functions of $\beta_{\rm ic,b}$ for all model sequences, varying from near uniform rotation ($A5$) to strong differential rotation ($A1$). $J_{\rm ic,b}$ increases linearly with $\beta_{\rm ic,b}$ and, for $\beta_{\rm ic,b} \lesssim 0.12$, is nearly independent of the degree of differential rotation. $M_{\rm ic,b}$ also increases with $\beta_{\rm ic,b}$ (and $J_{\rm ic,b}$) and is essentially independent of differential rotation for $\beta_{\rm ic,b} \lesssim 0.18$.

rotational energy. Hence, at fixed $\beta_{\rm ic,b}$ and $M_{\rm ic,b}$, $J_{\rm ic,b}$ for a model with smaller A will be smaller.

The central rest-mass density is important for the structure and dynamics of the inner core, which turns into the unshocked protoneutron star core after bounce. In the nonrotating, low-temperature limit, the central density, for a given nuclear EOS, determines stellar structure and pulsational mode spectrum completely [86]. In Fig. 5, we plot the central density at bounce ($\rho_{\rm c,b}$ as a function of $\beta_{\rm ic,b}$; upper graphs) and the time-averaged density over the first few milliseconds after bounce ($\rho_{\rm max,pb}$ as a function of $\beta_{\rm ic,pb}$; lower graphs; we average over 6 ms, from 2 to 8 ms after bounce). Both quantities decrease with increasing total rotation, since centrifugal support keeps the core in a less compact (i.e., lower-density) configuration. The central densities of very slowly rotating models ($\beta_{\rm ic,b} \lesssim 0.02$–$0.03$) exhibit little variation with differential rotation parameter A. In more rapidly rotating models, those with smaller A (more differential rotation) have systematically slightly larger $\rho_{\rm c,b}$. Since most of their spin is concentrated at small radii (and mass coordinates), they experience less centrifugal support throughout the collapsing inner core than models with

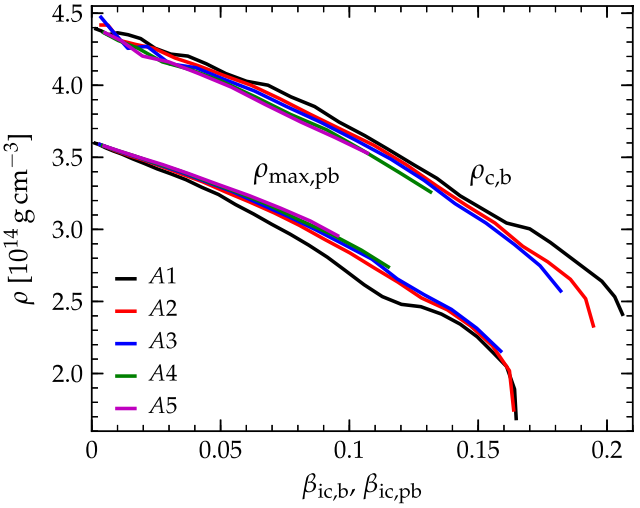

FIG. 5 (color online). The central rest-mass density at bounce $\rho_{\rm c,b}$ as a function of $\beta_{\rm ic,b}$ (upper graphs) and time-average maximum density in the postbounce phase $\rho_{\rm c,pb}$ as a function of the time-averaged $\beta_{\rm ic,pb}$ (lower graphs). We show curves for the five values of the differential rotation parameter A. Centrifugal support leads to a decrease in the density both at bounce and in the postbounce core. A strong dependence on differential rotation is apparent only in very rapidly rotating models. Note that differentially rotating models develop slightly off-center density maxima and quasitoroidal structure (cf. Fig. 6), but the maximum density exceeds the central density only by a few percent in such models.

larger A at the same $\beta_{\rm ic,b}$. However, after bounce the extremely rapid rotation in the central regions of strongly differentially spinning models leads to slightly more oblate innermost cores and somewhat lower time-average postbounce densities, as shown by Fig. 5.

Figure 6 depicts two-dimensional entropy colormaps with superposed isodensity contours at 12 ms after bounce for three representative models with $\beta_{\rm ic,b} \sim 0.1$ and differential rotation parameters $A1$ (model $A1O9$, strong differential rotation), $A3$ (model $A3O6$, moderate differential rotation), and $A5$ (model $A5O5.5$, nearly uniform rotation). Shown is the upper hemisphere and the rotation axis is aligned with the positive z-axis. The unshocked protoneutron star core (specific entropy $s \lesssim 3k_{\rm B}$ baryon^{-1}) is more extended in less differentially rotating models, since these have more angular momentum at larger mass (and radial) coordinate.

Figure 6 also shows that overall shape of the protoneutron star cores varies with differential rotation. While the $A5$ model is clearly spheroidal, the density contours (traced by the entropy distribution) of the strongly differentially rotating $A1$ model show a double-lobed structure characteristic of quasitoroidal equilibrium configurations that have their maximum density not at a single point at the origin, but in a ring at some finite radius in the equatorial plane. This is expected to occur in strongly differentially rotating cores and has been reported before in, e.g., [37,39,48,50].

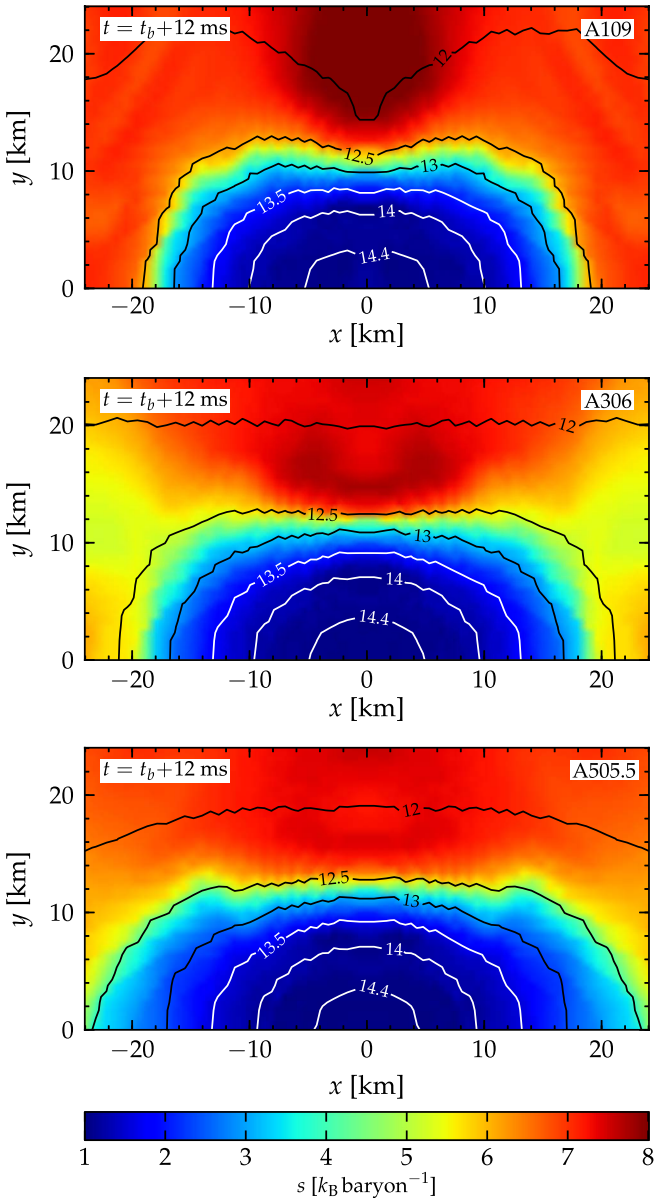

FIG. 6 (color online). Entropy colormaps of the meridional plane for models $A1O9$, $A3O6$, $A5O5.5$ with $\beta_{\rm ic,b} \sim 0.1$ at 12 ms after bounce. Black and white lines are mark density isocontours at 10^{12}, $10^{12.5}$, 10^{13}, $10^{13.5}$, 10^{14}, and 1. More differentially rotating models have more compact unshocked (low entropy) cores and more centrifugally deformed innermost density isocontours.

We indeed find that the tendency to develop off-center density maxima increases with decreasing A, but even the most rapidly differentially rotating model in our entire set has a density contrast of only $\rho_{\rm max,pb}/\rho_{\rm c,pb} - 1 \lesssim 3\%$, and its density maximum is located only ∼1.2 km off the origin.

In Fig. 7, we plot the evolution of the central density of the same three models ($A1O9$, $A3O6$, and $A505.5$) with $\beta_{\rm ic,b} \sim 0.1$ shown in Fig. 6. At bounce, the most differentially rotating model overshoots its postbounce quasiequlibrium the most, settles at the lowest $\rho_{\rm c,pb}$, and exhibits

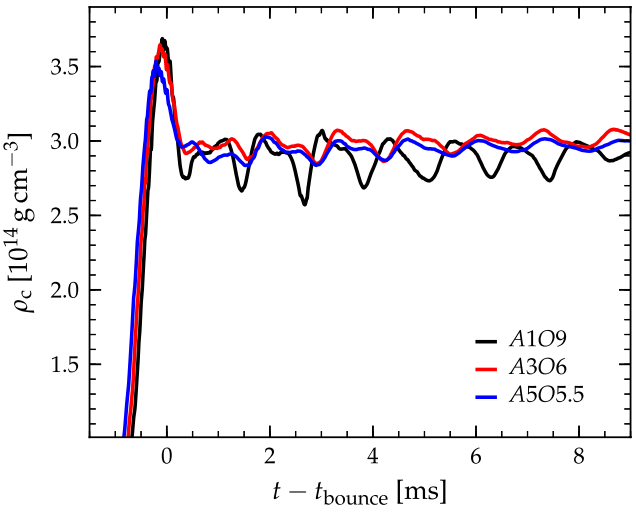

FIG. 7 (color online). Time evolution of the central density for models $A1O9$, $A3O6$, and $A5O5.5$, all of which have $\beta_{\rm ic,b} \sim 0.1$. More differentially rotating models more strongly overshoot their postbounce quasiequilibrium central densities at bounce and exhibit stronger postbounce ring-down oscillations.

the strongest postbounce ring-down oscillations. These oscillations are nonlinear and a superposition of multiple modes, but, in previous work, at least one of the modes has been identified as the fundamental quadrupole mode of the protoneutron star core [38]. The most differentially rotating model has most of its spin concentrated in the innermost regions. Hence, these regions are most oblate ($\ell = 2$) in this model, yielding the strongest excitation of the quadrupole core pulsation mode.

In summary and to connect to the next section on GW emission, although the important quantities $\rho_{\rm c,b}$ and $\rho_{\rm max\ or\ c,pb}$ depend primarily on $\beta_{\rm ic,b}$, we also observe a dependence on the differential rotation parameter A, in particular in rapidly rotating cases. This and the obvious differences in the two-dimensional structure of the postbounce cores shown in Fig. 6 suggest that the detailed multidimensional dynamics of the GW-emitting inner core is governed not only by its total rotation, but also by the distribution of angular momentum. We shall next investigate the effect of differential rotation on the GW signal.

B. Influence of differential rotation on the gravitational wave signal

For an analysis of the influence of the differential rotation parameter A on the GW signal, it is useful to first recap the latter's general morphology and at which point in the highly dynamical evolution of the inner core it reaches its peak values. In the following, without loss of generality, we will assume that the core's spin is aligned with the positive z-axis. The bottom panel of Fig. 2 shows the GW strain h_+ (there is only one polarization due to axisymmetry) as a function of time in the late collapse, bounce, and early postbounce phases of our reference model $A3O6$. During the collapse phase, h increases slowly and reaches a positive peak, $h_{1,\rm pos}$, during the rapid contraction phase immediately before bounce. During bounce, h decreases rapidly, reaching its most pronounced negative peak $h_{1,\rm neg}$ when the inner core is expanding at bounce (cf. the evolution of the maximum density shown in the top panel of Fig. 2). Following $h_{1,\rm neg}$, h reaches positive values and generically has a new positive local maximum, $h_{2,\rm pos}$. In slowly rotating models ($\beta_{\rm ic,b} \lesssim 0.05$), $h_{2,\rm pos}$ coincides with the first recontraction of the core after bounce. In the rapidly rotating case, an identification of $h_{2,\rm pos}$ with global core dynamics is less obvious, since bounce leads to the excitation of several oscillation modes in the core (dominated by the fundamental quadrupole mode; see [38]), which all contribute to the GW signal at this point. After $h_{2,\rm pos}$, the core undergoes ring-down oscillations that are damped hydrodynamically. They produce more peaks in h whose amplitudes decay on a timescale of 10–15 ms. Hereafter, we refer to the peaks that occur after $h_{1,\rm neg}$ as ring-down peaks.

Hayama *et al.* [87] analyzed two-dimensional Newtonian simulations of 12 models simulated by Kotake *et al.* [49] with varying rotation law and degrees of total and differential rotation. They studied the peak values of GW strain and observed that the ring-down peak with the largest absolute value—which we denote as H hereafter—is negative ($H < 0$) for models with rapid differential rotation [and a cylindrical rotation law like our Eq. (1)], while for the rest of their models H is positive and coincides with $h_{2,\rm pos}$. They argued that the detection and extraction of the sign of H could therefore provide clear information about the angular momentum distribution in the progenitor's core.

Figure 8 displays H as a function of $\beta_{\rm ic,b}$ for different values of A for all of our models. H grows almost linearly with $\beta_{\rm ic,b}$ for $\beta_{\rm ic,b} \lesssim 0.08$ for all values of A. In this regime, H is positive and corresponds to $h_{2,\rm pos}$. All values of A yield nearly identical H for a given $\beta_{\rm ic,b}$ for $\beta_{\rm ic,b} \lesssim 0.08$, implying that in this regime H is affected by the total rotation of the inner core but not by the distribution of angular momentum within the inner core.

In more rapidly rotating models ($\beta_{\rm ic,b} \gtrsim 0.08$), the values of H diverge for different A with the general trend that more differentially rotating models yield larger positive H. At $\beta_{\rm ic,b} \gtrsim 0.12$, H becomes negative and no longer corresponds to $h_{2,\rm pos}$. This occurs first (in $\beta_{\rm ic,b}$) for less differentially rotating models and the most differentially rotating sequence $A1$ maintains positive H with only a single outlier in which a negative peak has a just slightly (by ~0.5%) larger magnitude than $h_{2,\rm pos}$. From this, we conclude that the sign of H is not a good indicator for differential rotation. This is in disagreement with the statement made by Hayama *et al.* [87], who drew their conclusions on the basis of a smaller set of models that explored the parameter

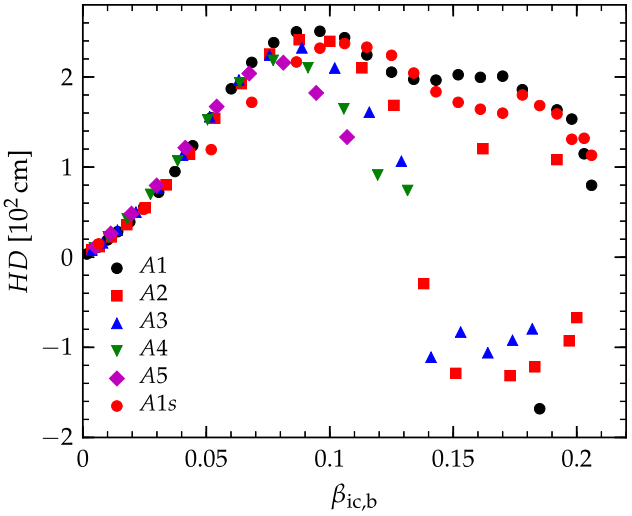

FIG. 8 (color online). Values of the second largest peak (in absolute value) H of the GW signal as a function of $\beta_{\rm ic,b}$ for all models (shown is the rescaled quantity HD, where D is the distance source). Models $A1$–$A5$ are simulated with the Lattimer-Swesty EOS [62], while a subset of rapidly differentially rotating models from sequence $A1$, which we refer to as sequence $A1s$ (shown with red circles), is simulated with the Shen *et al.* [60,61] EOS. More differentially rotating models yield larger positive H and switch to negative H at higher $\beta_{\rm ic,b}$. While differential rotation is a necessary criterion for $H < 0$, it is not a sufficient one.

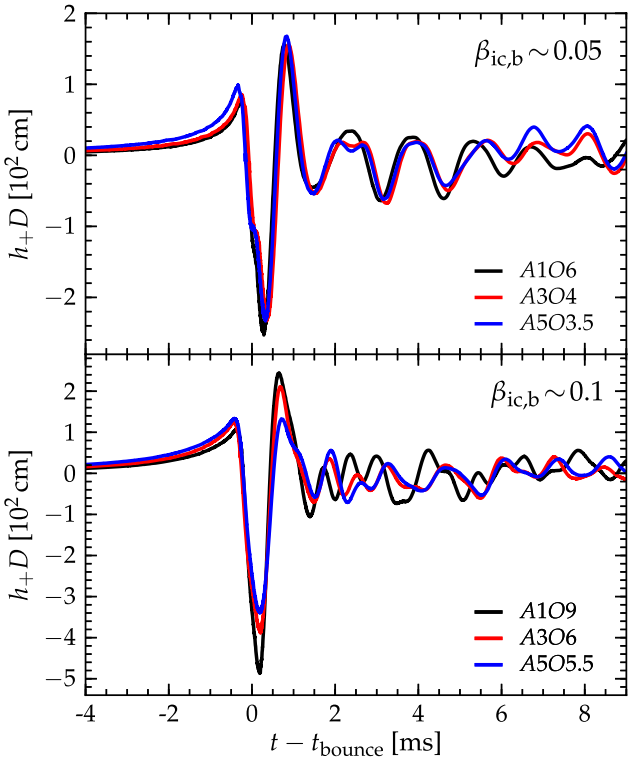

FIG. 9 (color online). GW strain h_+ rescaled by source distance D. The top panel shows three models with different degrees of differential rotation but with the same $\beta_{\rm ic,b} \sim 0.05$. The bottom panel shows three more rapidly spinning models with $\beta_{\rm ic,b} \sim 0.1$. In the first case, the three models exhibit almost identical GW signals from bounce, suggesting little sensitivity to differential rotation. The situation is different in the rapid rotation case, where there is significant variation between models with different values of the differential rotation parameter A.

space less systematically than our model sequences. In their defense, we note that $H < 0$ occurs only in models which have at least weak differential rotation ($A \lesssim A3$ in our model set), simply because uniformly spinning models cannot reach sufficiently high $\beta_{\rm ic,b}$ for H to become negative (Figs. 3 and 8). However, the opposite is not true, since $H > 0$ does not always indicate uniform rotation.

In order to further underpin the above conclusion that the sign of H is not a good indicator for differential rotation, we carry out additional simulations of the subset of rapidly rotating models from the most differentially rotating model sequence A1. These simulations use the EOS of Shen *et al.* [60,61] instead of the Lattimer and Swesty EOS [62] and we call this model set $A1s$. The Shen *et al.* EOS is the EOS used by the models underlying the Hamaya *et al.* study [87]. These additional simulations thus allow us to exclude potential ambiguities due to the use of a different EOS. The values of H of the simulations with the Shen *et al.* EOS are marked by red circles in Fig. 8. They are positive for all simulated models. This supports our conclusion that H is not necessarily negative in strongly differentially rotating models and thus not a solid indicator of the strength of differential rotation.

In Fig. 9, we compare waveforms of models with the same total rotation (as measured by $\beta_{\rm ic,b}$) but different degrees of differential rotation. The top panel depicts waveforms of models with moderate rotation ($\beta_{\rm ic,b} \sim 0.05$) while the bottom panel shows waveforms of rapidly spinning models with $\beta_{\rm ic,b} \sim 0.10$. At $\beta_{\rm ic,b} \sim 0.05$, all choices of A yield essentially the same waveform between peaks $h_{1,\rm pos}$ and $h_{2,\rm pos}$ and differences appear only during the ring-down phase. The situation is different for rapidly rotating models whose dynamics is more strongly affected by rotation. While the overall shape of the bounce spike and its width are still the same for all values of A, more differentially rotating models yield larger $|h_{1,\rm neg}|$ and $h_{2,\rm pos}$. The ring-down waveform of the most differentially rotating model is very different from the other models, reflecting the much more pronounced postbounce variations in its central density shown in Fig. 7.

The trends seen for the few select models shown in Fig. 9 for the bounce part of the waveform are very systematic. This is revealed by Fig. 10, which shows the values of $h_{1,\rm pos}$, $h_{1,\rm neg}$, $h_{2,\rm pos}$, and $h_{2,\rm neg}$ as a function of $\beta_{\rm ic,b}$ for the five considered choices of differential rotation parameter A. At slow rotation ($\beta_{\rm ic,b} \lesssim 0.04$–$0.08$) there is little dependence on differential rotation. In more rapidly rotating models, increasing differential rotation (= decreasing A) systematically decreases $h_{1,\rm pos}$, makes $h_{1,\rm neg}$ more negative,

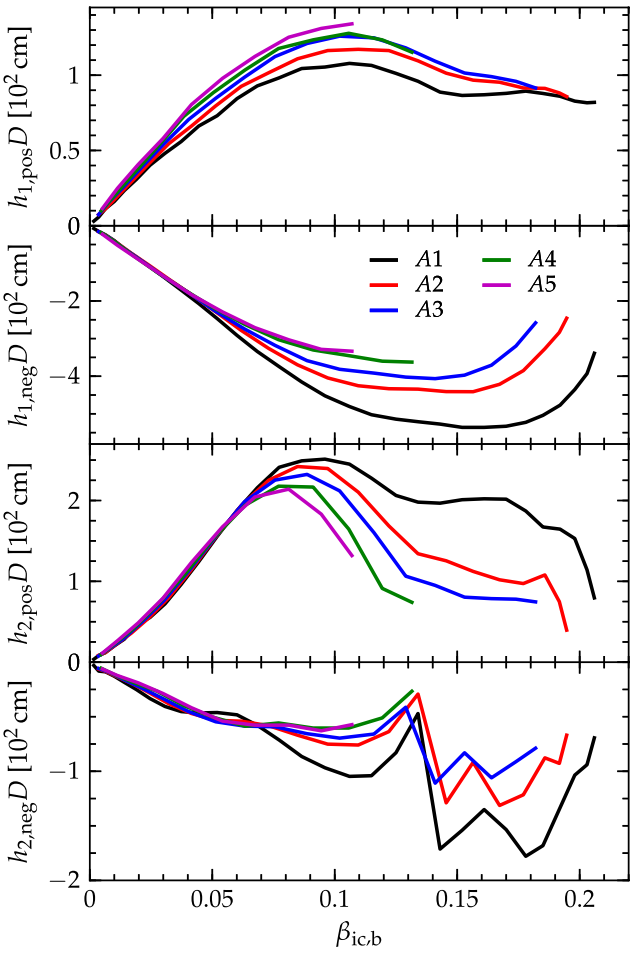

FIG. 10 (color online). The values of the first three peaks of the GW strain $h_{1,\mathrm{pos}}$, $h_{1,\mathrm{neg}}$, $h_{2,\mathrm{pos}}$ (cf. Fig. 2) as a function of $\beta_{\mathrm{ic,b}}$ plotted for all five model sequences. These three prominent GW signal peaks are insensitive to the angular momentum distribution for slowly rotating models that reach $\beta_{\mathrm{ic,b}} \lesssim 0.04$–$0.08$. More rapidly rotating models show clear trends with differential rotation.

and increases $h_{2,\mathrm{pos}}$. This suggests that it should—in principle—be possible to infer the degree of differential rotation of rapidly rotating cores from the GW signal alone. In Sec. V, we explore two methods that can be used to "measure" total rotation and A from an observed signal.

V. RESULTS: EXTRACTING THE ANGULAR MOMENTUM DISTRIBUTION FROM AN OBSERVED SIGNAL

A. Numerical template bank analysis

As our analysis in the previous section suggests, many characteristics of both the dynamics and GW emission associated with rotating core-collapse supernovae are dependent on both total rotation (expressed in $\beta_{\mathrm{ic,b}}$) and the degree of differential rotation given by parameter A. In the following, we carry out a matched filter analysis to assess the dependence of all signal features on $\beta_{\mathrm{ic,b}}$ and A and to study how well we can hope to extract total and differential rotation from an observed signal. In the case of a known signal in Gaussian noise, it has been shown that matched filtering is the optimal detection technique [88]. This approach cross correlates the GW data observed with a series of filter waveforms, known as templates, produced from GW emission models for the targeted source.

Generally, GWs from core-collapse supernovae are not amenable to matched filtering analysis, since turbulence in the protoneutron star and behind the stalled shock provides a stochastic component to the signal [89,90]. However, in the case of rapid rotation, convection is suppressed by a stabilizing positive specific angular momentum gradient in the postshock region (e.g., [91]) and does not contribute significantly to the GW emission, in particular, not at bounce and in the first few milliseconds after bounce. Hence, the signal from rotating collapse, bounce, and postbounce ring down can be modeled deterministically and with high precision for a given EOS and neutrino treatment and matched filtering can be applied.

We construct a numerical template bank, utilizing the GW signals from all models described in Table I (see Table II for a summary of quantitative results) as templates to filter observed GW data. Using the known GW waveform expected from each model and the detector's noise statistics, we find the best-fitting template for each signal. We consider signal waveforms not used as templates in order to imitate the "real-life" situation where the observed GW signal is not exactly known. For all values of A, we use injections spanning the template parameter space, with values of Ω_{c} differing from those of the templates by at least 0.25 rad s^{-1}. As $\beta_{\mathrm{ic,b}}$ and A for all templates are known, finding the best-fitting template for an injected

TABLE I. Summary of key parameters of our model sequences. $\Omega_{\mathrm{c,max}}$ is the central angular velocity corresponding to the fastest spinning model in each A-sequence. $\beta_{\mathrm{ic,b,min}}$ and $\beta_{\mathrm{ic,b,max}}$ are the values of $\beta = T/|W|$ of the inner core at bounce for the slowest and fastest rotators of each sequence, respectively. Note that $\Omega_{\mathrm{c,max}}$ and $\beta_{\mathrm{ic,b,max}}$ in the only mildly differentially rotating sequence $A4$ and $A5$ are limited by the fact that more rapidly spinning models fail to collapse. In more differentially rotating models, $\Omega_{\mathrm{c,max}}$ is the value for which we obtain $\beta_{\mathrm{ic,b,max}}$. Due to centrifugal effects, models with higher initial Ω_{c} yield smaller $\beta_{\mathrm{ic,b}}$ (see Fig. 4, and, e.g., [26,37,52]).

Model sequence	A [km]	$\Omega_{\mathrm{c,min}}$ [rad s-1]	$\Omega_{\mathrm{c,max}}$ [rads-1]	$\beta_{\mathrm{ic,b,min}}$ [10^{-2}]	$\beta_{\mathrm{ic,b,max}}$	Number of models
*A*1	300	1	15.5	1.62	0.21	30
*A*2	417	1	11.5	3.13	0.19	22
*A*3	634	1	9.5	3.58	0.18	18
*A*4	1268	1	6.5	4.66	0.13	12
*A*5	10000	1	5.5	5.15	0.11	10

TABLE II. Summary of simulation results. Ω_c is the intitial central angular velocity, $\rho_{c,b}$ is the central density at bounce, $\rho_{c,pb}$ is the early postbounce central density, $\rho_{max,pb}$ is the postbounce maximum density, and $\beta_{ic,b}$ and $\beta_{ic,pb}$ are ratios of the rotational kinetic energy to the gravitational binding energy of the inner core at bounce and early postbounce phase, respectively. β_i is the initial value of β. $M_{ic,b}$ and $J_{ic,b}$ are the inner core mass and angular momentum at bounce, $|h_{+,2}|D$ is the second peak of the GW signal, while $|h_{+,max}|D$ is its maximum value. f_{max} is the frequency at which the GW spectral energy density reaches a maximum value. The optimal SNR at 10 kpc is the signal-to-noise ratio that would be seen by Advanced LIGO at design sensitivity, for a source located at 10 kpc. The symbol $*$ at the end of the model name indicates that for this model the peak GW signal is produced by convection. All waveforms are available for download from http://www.stellarcollapse.org.

Model	Ω_c [rad s^{-1}]	β_i [10^{-2}]	$\rho_{c,b}$ [10^{14} g cm^{-3}]	$\rho_{c,pb}$ [10^{14} g cm^{-3}]	$\rho_{max,pb}$ [10^{14} g cm^{-3}]	$\beta_{ic,b}$ [10^{-2}]	$\beta_{ic,pb}$ [10^{-2}]	$M_{ic,b}$ [$M_\odot$]	$J_{ic,b}$ [10^{48} erg s]	HD [cm]	$\lvert h_{+,max}\rvert D$ [cm]	E_{GW} [$10^{-9} M_\odot c^2$]	f_{max} [Hz]	Optimal SNR @ 10 kpc
*A1O1**	1.0	0.005	4.39	3.60	3.60	0.16	0.13	0.58	0.31	3.55	7.38	7.19	829.17	76.51
*A1O1.5**	1.5	0.010	4.38	3.59	3.59	0.36	0.30	0.58	0.46	8.20	15.30	8.62	821.17	80.42
*A1O2**	2.0	0.018	4.35	3.57	3.57	0.64	0.53	0.59	0.63	11.41	24.29	9.02	937.69	83.56
*A1O2.5**	2.5	0.028	4.36	3.55	3.55	1.00	0.82	0.58	0.77	19.23	39.67	6.26	817.92	66.13
*A1O3**	3.0	0.041	4.35	3.52	3.52	1.41	1.17	0.58	0.92	28.33	61.77	7.86	842.68	76.27
A1O3.5	3.5	0.055	4.32	3.49	3.49	1.90	1.58	0.59	1.11	39.25	83.27	6.75	824.79	68.43
A1O4	4.0	0.072	4.26	3.46	3.46	2.46	2.04	0.61	1.37	54.99	109.77	8.90	764.99	64.93
A1O4.5	4.5	0.092	4.22	3.42	3.42	3.07	2.54	0.61	1.50	72.04	138.94	12.01	833.67	72.16
A1O5	5.0	0.113	4.20	3.39	3.39	3.73	3.08	0.61	1.67	95.10	171.21	12.60	678.00	72.77
A1O5.5	5.5	0.137	4.15	3.34	3.35	4.45	3.66	0.65	1.99	123.68	207.07	19.05	681.96	67.64
A1O6	6.0	0.163	4.08	3.29	3.29	5.20	4.27	0.65	2.17	154.79	246.82	31.39	716.50	79.69
A1O6.5	6.5	0.191	4.03	3.24	3.25	6.01	4.92	0.65	2.39	186.88	291.49	38.88	816.62	90.79
A1O7	7.0	0.222	4.00	3.17	3.18	6.84	5.58	0.67	2.69	216.14	334.38	44.36	764.27	89.98
A1O7.5	7.5	0.255	3.92	3.11	3.12	7.73	6.28	0.68	2.94	238.11	374.54	59.05	786.14	113.81
A1O8	8.0	0.290	3.85	3.04	3.06	8.65	6.98	0.70	3.24	250.10	415.24	66.28	811.45	115.69
A1O8.5	8.5	0.327	3.74	2.97	3.00	9.60	7.70	0.70	3.50	250.68	452.12	73.11	834.94	108.89
A1O9	9.0	0.367	3.65	2.89	2.93	10.60	8.42	0.72	3.87	243.61	480.53	80.65	844.19	138.00
A1O9.5	9.5	0.409	3.56	2.81	2.85	11.50	9.14	0.74	4.17	224.49	502.39	86.60	827.66	145.97
A1O10	10.0	0.453	3.45	2.71	2.77	12.50	9.85	0.74	4.52	205.33	514.13	87.51	562.73	147.72
A1O10.5	10.5	0.499	3.35	2.62	2.69	13.40	10.57	0.76	4.92	197.37	520.96	86.21	560.75	160.32
A1O11	11.0	0.548	3.23	2.53	2.61	14.30	11.28	0.78	5.28	196.45	527.25	78.28	504.13	151.77
A1O11.5	11.5	0.599	3.14	2.48	2.55	15.20	12.02	0.79	5.71	202.47	535.99	76.40	483.85	159.97
A1O12	12.0	0.652	3.04	2.46	2.50	16.10	12.78	0.80	6.15	199.54	535.99	74.46	483.08	162.68
A1O12.5	12.5	0.707	3.00	2.41	2.44	17.00	13.57	0.82	6.63	200.88	532.98	70.81	477.07	158.29
A1O13	13.0	0.765	2.91	2.34	2.37	17.80	14.30	0.84	7.10	185.89	522.60	62.99	448.28	171.52
A1O13.5	13.5	0.825	2.82	2.25	2.28	18.50	14.96	0.85	7.58	−168.14	504.03	50.41	433.69	164.50
A1O13	14.0	0.887	2.72	2.15	2.18	19.20	15.55	0.86	8.06	163.46	476.98	37.97	387.50	161.12
A1O14.5	14.5	0.952	2.64	2.05	2.08	19.80	16.10	0.89	8.69	153.26	435.46	25.70	375.43	150.47
A1O15	15.0	1.018	2.53	1.89	1.92	20.30	16.41	0.91	9.33	114.74	393.11	17.24	319.46	140.08
A1O15.5	15.5	1.087	2.41	1.69	1.72	20.60	16.47	0.94	10.24	79.77	339.02	11.41	271.36	130.90
*A2O1**	1.0	0.011	4.42	3.59	3.59	0.36	0.31	0.57	0.44	8.47	16.12	17.36	851.53	99.46
*A2O1.5**	1.5	0.025	4.42	3.57	3.57	0.63	0.54	0.58	0.61	11.82	24.91	16.34	859.90	74.77
*A2O2**	2.0	0.044	4.31	3.54	3.55	1.10	0.95	0.58	0.81	22.59	45.35	7.59	837.97	70.49
*A2O2.5**	2.5	0.069	4.28	3.51	3.51	1.70	1.46	0.59	1.04	36.18	73.49	16.82	777.70	80.73
A2O3	3.0	0.099	4.26	3.48	3.48	2.42	2.06	0.61	1.31	55.02	104.90	8.57	853.71	71.84

(Table continued)

TABLE II. (*Continued*)

Model	Ω_c [rad s^{-1}]	β_i [10^{-2}]	$\rho_{c,b}$ [10^{14} g cm^{-3}]	$\rho_{c,pb}$ [10^{14} g cm^{-3}]	$\rho_{max,pb}$ [10^{14} g cm^{-3}]	$\beta_{ic,b}$ [10^{-2}]	$\beta_{ic,pb}$ [10^{-2}]	$M_{ic,b}$ [$M_\odot$]	$J_{ic,b}$ [10^{48} erg s]	HD [cm]	$\lvert h_{+,max}\rvert D$ [cm]	E_{GW} [$10^{-9} M_\odot c^2$]	f_{max} [Hz]	Optimal SNR @ 10 kpc
A2O3.5	3.5	0.134	4.19	3.43	3.43	3.23	2.74	0.61	1.51	80.32	142.33	11.67	745.77	74.43
A2O4	4.0	0.175	4.14	3.38	3.39	4.14	3.49	0.63	1.86	114.50	182.76	14.81	687.60	62.25
A2O4.5	4.5	0.222	4.07	3.33	3.33	5.13	4.31	0.64	2.12	154.00	228.38	26.08	827.37	75.95
A2O5	5.0	0.274	4.00	3.26	3.26	6.18	5.18	0.65	2.46	192.64	278.38	34.18	696.93	78.45
A2O5.5	5.5	0.332	3.91	3.19	3.19	7.30	6.12	0.67	2.85	225.44	326.18	45.00	732.25	107.09
A2O6	6.0	0.395	3.80	3.11	3.12	8.48	7.08	0.70	3.25	241.38	369.89	54.82	763.68	120.96
A2O6.5	6.5	0.463	3.69	3.03	3.03	9.71	8.06	0.72	3.72	239.45	404.59	58.80	782.64	111.90
A2O7	7.0	0.537	3.58	2.93	2.94	10.96	9.03	0.72	4.09	210.17	425.35	60.28	797.74	114.80
A2O7.5	7.5	0.617	3.45	2.84	2.86	12.21	10.02	0.74	4.52	168.37	433.27	59.28	814.41	114.98
A2O8	8.0	0.702	3.30	2.73	2.75	13.40	10.95	0.76	5.00	−29.23	434.36	53.48	820.71	123.51
A2O8.5	8.5	0.792	3.17	2.63	2.65	14.55	11.88	0.78	5.63	−128.94	440.92	47.17	828.62	125.06
A2O9	9.0	0.888	3.04	2.52	2.54	15.65	12.80	0.80	6.35	120.47	441.19	40.59	830.37	124.23
A2O9.5	9.5	0.989	2.88	2.44	2.45	16.73	13.80	0.82	6.90	−131.32	421.52	32.56	394.97	126.22
A2O10	10.0	1.096	2.77	2.33	2.34	17.70	14.70	0.84	7.62	−121.56	385.19	21.90	373.13	130.38
A2O10.5	10.5	1.209	2.65	2.19	2.20	18.58	15.55	0.86	8.37	108.38	327.00	14.20	330.47	126.41
A2O11	11.0	1.326	2.52	2.02	2.03	19.17	16.21	0.87	9.05	−92.77	283.57	8.98	292.98	117.20
A2O11.5	11.5	1.450	2.33	1.75	1.76	19.47	16.38	0.89	9.76	−66.93	245.87	5.39	216.11	104.68
*A3O1**	1.0	0.018	4.47	3.59	3.59	0.36	0.31	0.57	0.45	7.55	15.84	7.05	873.82	110.38
*A3O1.5**	1.5	0.042	4.38	3.56	3.57	0.80	0.70	0.58	0.69	15.96	32.13	8.62	850.91	74.83
*A3O2**	2.0	0.074	4.26	3.53	3.53	1.40	1.23	0.59	0.94	29.95	60.87	4.04	798.47	71.14
*A3O2.5**	2.5	0.115	4.27	3.49	3.50	2.15	1.88	0.61	1.24	49.99	94.90	6.50	772.97	72.30
A3O3	3.0	0.166	4.15	3.45	3.45	3.03	2.63	0.60	1.45	76.27	135.69	16.04	873.48	72.33
A3O3.5	3.5	0.226	4.12	3.40	3.40	4.04	3.48	0.63	1.82	112.95	178.53	14.12	718.34	69.98
A3O4	4.0	0.295	4.04	3.33	3.33	5.14	4.41	0.65	2.18	155.85	227.84	23.05	706.91	67.38
A3O4.5	4.5	0.374	3.96	3.27	3.27	6.32	5.42	0.66	2.55	196.67	274.55	34.01	706.90	94.83
A3O5	5.0	0.462	3.85	3.18	3.18	7.56	6.48	0.68	2.98	223.97	317.99	44.21	725.72	98.87
A3O5.5	5.5	0.558	3.74	3.09	3.10	8.87	7.59	0.70	3.40	232.28	358.69	49.45	749.09	97.50
A3O6	6.0	0.665	3.62	3.00	3.00	10.20	8.70	0.71	3.81	209.89	381.64	49.92	767.59	97.51
A3O6.5	6.5	0.780	3.49	2.89	2.90	11.60	9.80	0.73	4.40	160.80	391.75	48.03	780.76	102.94
A3O7	7.0	0.905	3.34	2.79	2.80	12.90	10.88	0.75	4.92	106.38	402.40	43.74	795.01	107.17
A3O7.5	7.5	1.038	3.18	2.66	2.67	14.10	11.86	0.77	5.60	−110.93	406.50	36.92	799.64	107.30
A3O8	8.0	1.182	3.04	2.55	2.56	15.30	12.90	0.79	6.31	−83.05	397.21	31.53	797.59	108.76
A3O8.5	8.5	1.334	2.90	2.44	2.45	16.40	13.96	0.81	7.02	−106.00	370.71	22.83	792.28	110.54
A3O9	9.0	1.496	2.75	2.31	2.32	17.40	14.94	0.83	7.74	−92.34	319.63	13.36	371.50	109.63
A3O9.5	9.5	1.666	2.57	2.16	2.16	18.20	15.87	0.85	8.61	−79.50	258.16	7.88	285.59	104.34
*A4O1**	1.0	0.048	4.36	3.58	3.58	0.47	0.42	0.57	0.51	10.24	18.49	4.18	871.56	60.29
*A4O1.5**	1.5	0.108	4.31	3.55	3.55	1.03	0.95	0.58	0.78	22.79	43.16	3.66	971.44	55.68
*A4O2**	2.0	0.192	4.26	3.51	3.51	1.80	1.65	0.60	1.10	42.41	80.59	6.42	808.24	64.09
*A4O2.5**	2.5	0.300	4.16	3.46	3.46	2.74	2.48	0.60	1.35	69.73	123.48	9.11	836.50	83.71
A4O3	3.0	0.432	4.11	3.41	3.41	3.84	3.43	0.63	1.75	106.88	169.65	11.64	731.20	51.22

(Table continued)

TABLE II. (*Continued*)

Model	Ω_c [rad s^{-1}]	β_i [10^{-2}]	$\rho_{c,b}$ [10^{14} g cm^{-3}]	$\rho_{c,pb}$ [10^{14} g cm^{-3}]	$\rho_{max,pb}$ [10^{14} g cm^{-3}]	$\beta_{ic,b}$ [10^{-2}]	$\beta_{ic,pb}$ [10^{-2}]	$M_{ic,b}$ [$M_\odot$]	$J_{ic,b}$ [10^{48} erg s]	HD [cm]	$\lvert h_{+,max}\rvert D$ [cm]	E_{GW} [$10^{-9} M_\odot c^2$]	f_{max} [Hz]	Optimal SNR @ 10 kpc
A4O3.5	3.5	0.589	4.03	3.33	3.33	5.05	4.49	0.64	2.12	152.62	218.27	20.80	700.07	69.57
A4O4	4.0	0.769	3.92	3.26	3.26	6.34	5.65	0.66	2.53	193.86	262.80	31.50	696.11	78.32
A4O4.5	4.5	0.973	3.80	3.17	3.17	7.71	6.86	0.67	2.90	218.41	302.96	39.80	717.07	82.81
A4O5	5.0	1.201	3.69	3.06	3.07	9.12	8.07	0.70	3.46	210.43	330.28	41.04	727.72	85.89
A4O5.5	5.5	1.453	3.54	2.97	2.97	10.57	9.30	0.72	4.05	164.73	345.31	38.68	748.63	91.59
A4O6	6.0	1.730	3.39	2.86	2.86	11.94	10.47	0.73	4.56	91.24	360.06	35.27	749.91	95.20
A4O6.5	6.5	2.030	3.26	2.74	2.74	13.15	11.51	0.75	5.20	74.03	362.52	31.14	759.49	96.17
A5O1[*]	1.0	0.164	4.36	3.58	3.58	0.52	0.48	0.58	0.54	11.49	22.67	3.85	299.25	84.62
A5O1.5[*]	1.5	0.369	4.31	3.54	3.55	1.13	1.07	0.58	0.81	26.30	52.18	4.01	855.35	65.92
A5O2[*]	2.0	0.655	4.20	3.50	3.50	1.97	1.84	0.60	1.14	48.33	88.98	5.42	850.52	63.19
A5O2.5	2.5	1.024	4.16	3.45	3.45	2.99	2.75	0.61	1.42	79.58	133.40	7.67	716.12	61.20
A5O3	3.0	1.475	4.08	3.39	3.39	4.15	3.77	0.63	1.57	121.51	183.31	13.83	703.91	54.63
A5O3.5	3.5	2.007	3.99	3.31	3.31	5.42	4.90	0.64	2.18	167.09	229.20	23.55	701.79	72.92
A5O4	4.0	2.622	3.87	3.24	3.24	6.74	6.10	0.67	2.67	203.87	270.92	33.99	712.85	77.31
A5O4.5	4.5	3.319	3.74	3.15	3.15	8.12	7.32	0.68	3.12	215.85	303.24	39.64	721.69	83.62
A5O5	5.0	4.099	3.64	3.06	3.06	9.45	8.49	0.70	3.61	182.27	328.64	37.84	739.29	87.18
A5O5.5	5.5	4.960	3.53	2.96	2.96	10.70	9.54	0.71	4.05	133.29	333.56	35.93	760.41	88.38

signal will infer its associated closest $\beta_{ic,b}$ and A. Hereafter, we will refer to this procedure as measuring of $\beta_{ic,b}$ and A.

We perform our analysis in Fourier space, due to frequency dependence and Gaussian statistics of the GW detector noise, $\tilde{n}$, which is colored by known one-sided power spectral density (PSD) $S_h(f)$. We model the GW detector data, $\tilde{d}$, assumed to be comprised of both some core-collapse supernova GW signal, $\tilde{h}(f;\vec{\lambda})$, and $\tilde{n}$ as

$$\tilde{d}_i = \tilde{h}(f_i;\vec{\lambda}) + \tilde{n}_i, \tag{2}$$

where i denotes the frequency bin index.

The parameter dependence of the GW signals considered here is encoded in $\vec{\lambda}$,

$$\vec{\lambda} = \{D, t_0, \iota, \xi, \theta, \phi, \psi\}, \tag{3}$$

where D is the source distance, t_0 is the time at which the GW signal arrives at the detector, and $(\iota, \xi, \theta, \phi, \psi)$ are source angles. Here, (ι, ξ) relate the preferred internal axes of the source to the location of the detector, (θ, ϕ) relate the preferred internal axes of the detector to the location of the source and ψ defines the relationship between the source and the detector, via the plane characterizing the polarization of emitted GWs [92].

Our goal is to establish the best-fitting template for the observed GW data. We construct the noise-weighted inner product, $\langle d, x^j\rangle$, for all templates $\tilde{x}^j(f)$ with the data, where j denotes template index in the catalog, as

$$\langle d, x^j\rangle = 2\max_{t_0}\int_{-\infty}^{\infty}\frac{\tilde{d}(f)\tilde{x}^j(f)^* e^{i2\pi f t_0}}{S_h(f)}\mathrm{d}f, \tag{4}$$

where $*$ denotes complex conjugation. We assume stationary, Gaussian detector noise. We numerically maximize this quantity over all possible t_0 using fast-Fourier transforms. From this, we compute the detection SNR for each template, ρ^j, as

$$\rho^j = \frac{\langle d, x^j\rangle}{\langle x^j, x^j\rangle^{1/2}}, \tag{5}$$

where $\langle x^j, x^j\rangle$ is the template norm. For the optimal case in which $h = x^j$, the expected signal SNR is simply $\langle x^j, x^j\rangle^{1/2}$. Given this quantity, we calculate the set of ρ^j across all templates to determine the best-fitting template, given the data observed. We define the best-fitting template as the template j producing the largest ρ^j, given an imposed detection threshold of $\rho_j \geq 8$ [93].

We utilize simulated Gaussian noise colored by the zero-detuned high power configuration of aLIGO [94], and, for simplicity, consider a single GW detector. We repeat all calculations with ten different realizations of detector noise

and report the averaged result. We assume that the source is optimally oriented, and located relative to the detector such that the observed GW strain, h, given by

$$h = h_+ F_+ + h_\times F_\times, \tag{6}$$

is maximized, where the antenna response functions, F_+ and $F_\times$, are given by

$$F_+ = \frac{1}{2}(1+\cos^2\theta)\cos 2\phi \cos 2\psi - \cos\theta \sin 2\phi \sin 2\psi, \tag{7}$$

$$F_\times = \frac{1}{2}(1+\cos^2\theta)\cos 2\phi \sin 2\psi + \cos\theta \sin 2\phi \cos 2\psi, \tag{8}$$

respectively, and h_+ is related to H_{20}, the $(l,m)=(2,0)$ mode of the GW multipole expansion [95], as

$$h_+ = \frac{1}{D}\sqrt{\frac{15}{32\pi}} H_{20} \sin^2\iota. \tag{9}$$

Due to the axisymmetric nature of the simulations presented here, h_+ is independent of ξ and all GW emission will be linearly polarized (i.e., $h_\times = 0$). In physical terms, these assumptions correspond to setting source angles $(\iota,\theta,\phi,\psi) = (\pi/2,0,0,0)$. We place all sources at a known distance $D = 10$ kpc, restricting our analysis to the Galactic locus.

To conclude the discussion of our numerical template bank analysis, we note that the nature of our analysis is fundamentally distinct from template banks used in the context of LIGO/Virgo GW searches for compact binary coalescences, which can produce templates "on the fly" for binary inspiral signals using post-Newtonian expressions for the GW strain for arbitrary system parameters [96]. The GW emission from rotating core collapse is complicated, dependent on many parameters, and has yet to be described phenomenologically. This means that the span of the numerical template bank across the simulation parameter space is limited to discrete samples, with template waveforms produced by simulations of core collapse. The nature of templates for binary inspirals also conveys that the phase of GW emission can be robustly predicted, whereas convection in the later postbounce stages of core collapse is largely stochastic, resulting in unpredictable waveform phase. This limits the predictive power of our analysis in slowly rotating models in which convection abounds. Additionally, the study presented here considers only two unknown progenitor parameters (A and $\beta_{\rm ic,b}$), while in reality the simulation parameter space is larger and also includes (but is not necessarily limited to) EOS and electron fraction parametrization.

1. Extraction of $\beta_{\rm ic,b}$

The upper panel of Fig. 11 shows $\beta_{\rm ic,b}$ measured for injected waveforms versus the true values of $\beta_{\rm ic,b}$ of those models. The dashed black line denotes the optimal case in which the measured and true $\beta_{\rm ic,b}$ are identical. The lower panel shows the relative deviation of $\beta_{\rm ic,b}$ from its correct value. For most injected waveforms, the value of $\beta_{\rm ic,b}$ measured lies within ~20% of the true value for the five values of A considered, with $\beta_{\rm ic,b}$ ranging from ~0.01 to ~0.2. The average relative deviation of measured $\beta_{\rm ic,b}$ from its true value is ~8% for all injected waveforms. The measurement error is largest in slowly spinning models (small $\beta_{\rm ic,b}$), because these emit GW signals with strong stochastic components from prompt postbounce convection.

The matched filter analysis can extract $\beta_{\rm ic,b}$ with good accuracy across a wide range of both total rotation and

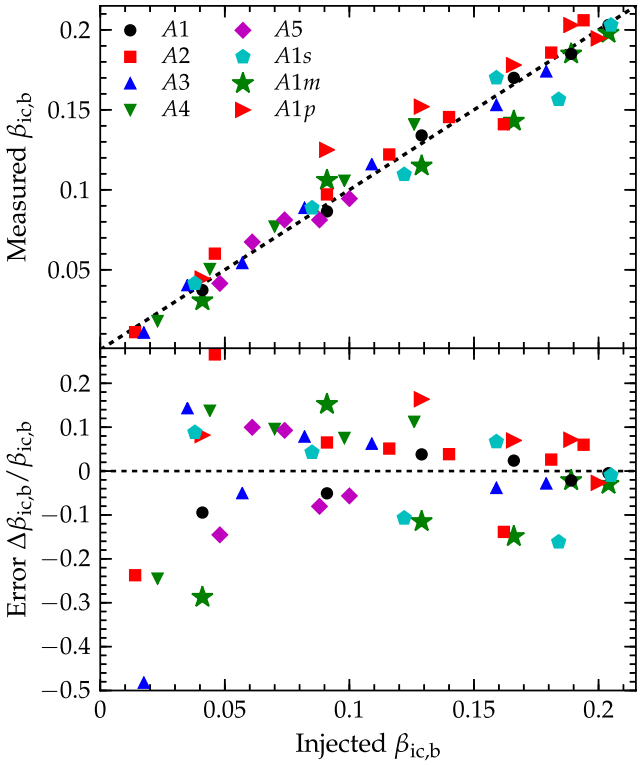

FIG. 11 (color online). Upper panel: Measured $\beta_{\rm ic,b}$ as a function of true $\beta_{\rm ic,b}$ for all injected waveforms. The dashed black line denotes the optimal case in which the measured and true $\beta_{\rm ic,b}$ are equal. Lower panel: The relative deviation of $\beta_{\rm ic,b}$ measured from its true value. For most signals, we find that $\beta_{\rm ic,b}$ is measured with ~10–20% accuracy. The errors are largest for slowly rotating models since these have strong stochastic convective components in their waveforms. Outliers at more rapid rotation are signals from the $A1s$, $A1m$, and $A1p$ injection sets. The $A1s$ models use the Shen *et al.* EOS [60,61] rather than the Lattimer-Swesty EOS [62] used for the fiducial models, while the $A1m$ and $A1p$ models are simulated with ~5% decreased and increased $Y_{\rm e}(\rho)$, respectively, at nuclear densities.

TABLE III. Summary of properties of models for injection. Ω_c is the intitial central angular velocity, $\rho_{c,b}$ is the central density at bounce, $\rho_{c,pb}$ is the early postbounce central density, $\rho_{max,pb}$ is the postbounce maximum density, $\beta_{ic,b}$ and $\beta_{ic,pb}$ are ratios of the rotational kinetic energy to the gravitational binding energy of the inner core at bounce and early postbounce phase, respectively. β_i is the initial value of β. $M_{ic,b}$ and $J_{ic,b}$ are the inner-core mass and angular momentum at bounce, $|h_{+,2}|D$ is the second peak of the GW signal, while $|h_{+,max}|D$ is its maximum value. f_{max} is the frequency at which the GW spectral energy density reaches a maximum value. The optimal SNR at 10 kpc is the signal-to-noise ratio that would be seen by Advanced LIGO at design sensitivity, for a source located at 10 kpc. All waveforms are available for download from http://www.stellarcollapse.org.

Model	Ω_c [rad s^{-1}]	β_i [10^{-2}]	$\rho_{c,b}$ [10^{14} g cm^{-3}]	$\rho_{c,pb}$ [10^{14} g cm^{-3}]	$\rho_{max,pb}$ [10^{14} g cm^{-3}]	$\beta_{ic,b}$ [10^{-2}]	$\beta_{ic,pb}$ [10^{-2}]	$M_{ic,b}$ [$M_\odot$]	$J_{ic,b}$ [10^{48} erg s]	HD [cm]	$\lvert h_{+,max}\rvert D$ [cm]	E_{GW} [$10^{-9} M_\odot c^2$]	f_{max} [Hz]	Optimal SNR @ 10 kpc
A1O5.25	5.25	0.12	4.28	3.37	3.37	4.09	3.36	0.63	1.83	111.19	189.59	16.19	991.53	67.91
A1O5.25m	5.25	0.12	4.18	3.41	3.41	4.04	3.38	0.60	1.68	93.98	163.91	23.23	950.30	74.67
A1O5.25p	5.25	0.12	4.18	3.30	3.30	4.14	3.33	0.60	1.96	132.49	213.63	14.33	864.48	81.89
A1O5.25s	5.25	0.12	3.33	2.65	2.65	3.79	3.15	0.60	1.72	87.97	158.17	11.41	687.21	60.11
A1O8.25	8.25	0.31	3.87	3.00	3.03	9.12	7.33	0.68	3.45	252.70	436.55	70.16	826.04	121.84
A1O8.25m	8.25	0.31	3.88	3.05	3.08	9.02	7.37	0.68	3.21	191.78	377.27	86.19	783.88	129.12
A1O8.25p	8.25	0.31	3.88	2.94	2.96	9.19	7.29	0.68	3.58	302.69	469.06	52.56	847.37	120.43
A1O8.25s	8.25	0.31	2.98	2.45	2.45	8.46	6.87	0.66	3.10	218.82	368.80	49.02	737.13	112.11
A1O10.25	10.25	0.48	3.42	2.65	2.72	12.90	10.20	0.76	4.81	199.43	521.24	87.74	645.55	159.93
A1O10.25m	10.25	0.48	3.45	2.75	2.80	12.80	10.20	0.74	4.59	180.30	490.37	93.17	541.00	167.36
A1O10.25p	10.25	0.48	3.45	2.59	2.65	13.00	10.10	0.74	4.92	228.11	540.91	74.00	922.20	140.51
A1O10.25s	10.25	0.48	2.76	2.22	2.26	12.20	9.64	0.72	4.45	211.99	492.01	73.49	795.74	122.64
A1O12.25	12.25	0.68	3.06	2.44	2.47	16.60	13.10	0.81	6.37	202.70	541.45	73.49	475.36	164.05
A1O12.25m	12.25	0.68	3.06	2.49	2.53	16.50	13.20	0.80	6.22	177.02	559.48	55.90	432.05	152.34
A1O12.25p	12.25	0.68	3.06	2.33	2.36	16.40	13.00	0.80	6.47	174.29	512.50	73.84	492.63	164.85
A1O12.25s	12.25	0.68	2.51	1.97	2.05	15.90	12.50	0.77	5.80	−171.29	522.33	66.92	486.68	137.42
A1O13.75	13.75	0.86	2.83	2.22	2.25	18.90	15.40	0.83	7.28	168.01	492.28	44.51	430.02	161.28
A1O13.75m	13.75	0.86	2.88	2.32	2.35	19.10	15.50	0.85	7.72	182.76	547.19	19.80	581.74	131.37
A1O13.75p	13.75	0.86	2.88	1.94	1.97	18.30	14.40	0.85	7.63	129.49	398.03	56.37	440.95	168.50
A1O13.75s	13.75	0.86	2.36	1.89	1.92	18.40	14.70	0.81	7.03	158.99	511.13	53.99	435.78	154.58
A1O15.25	15.25	1.05	2.49	1.79	1.82	20.40	16.50	0.88	9.00	94.80	369.07	13.96	275.55	135.89
A1O15.25m	15.25	1.05	2.61	2.06	2.10	21.10	17.60	0.89	9.19	160.36	469.33	6.77	221.11	126.96
A1O15.25p	15.25	1.05	2.49	1.16	2.10	19.40	14.50	0.89	9.09	−59.28	262.53	31.17	382.93	164.71
A1O15.25s	15.25	1.05	2.28	1.65	1.70	20.50	16.40	0.85	8.40	123.21	469.88	25.96	353.33	150.91
*A2O2.25**	2.25	0.06	4.28	3.53	3.53	1.50	1.18	0.16	0.92	30.32	61.47	14.28	846.22	68.47
A2O4.25	4.25	0.20	4.09	3.36	3.36	4.80	3.90	0.34	1.99	135.50	208.99	20.17	708.47	78.09
A2O6.25	6.25	0.43	3.76	3.07	3.08	9.30	7.58	0.59	3.05	244.77	388.74	56.97	772.26	111.00
A2O7.25	7.25	0.58	3.52	2.88	2.90	11.90	9.53	0.73	4.31	191.78	432.45	60.04	795.76	110.38
A2O8.25	8.25	0.75	3.23	2.67	2.69	14.40	11.39	0.77	5.32	132.49	441.19	50.47	827.73	123.82
A2O9.25	9.25	0.94	2.98	2.48	2.49	16.70	13.32	0.81	6.63	110.91	433.54	37.04	831.31	122.93
A2O10.25	10.25	1.15	2.73	2.27	2.28	18.70	15.20	0.85	8.00	107.36	357.87	17.62	331.04	128.63
A2O11.25	11.25	1.39	2.44	1.91	1.92	19.80	16.39	0.88	9.40	−82.78	267.99	6.90	276.56	110.52
*A3O2.25**	2.25	0.09	4.24	3.51	3.51	1.67	1.54	0.60	1.09	39.89	76.22	4.83	469.61	70.31
A3O3.25	3.25	0.20	4.14	3.42	3.42	3.30	3.04	0.62	1.64	94.52	158.99	17.38	880.87	65.11
A3O4.25	4.25	0.33	3.99	3.30	3.30	5.40	4.91	0.65	2.33	177.57	251.60	28.98	702.50	93.95
A3O5.25	5.25	0.51	3.80	3.14	3.14	7.70	7.03	0.69	3.19	231.39	340.39	47.44	741.09	97.12

(Table continued)

TABLE III. (*Continued*)

Model	Ω_c [rad s^{-1}]	β_i [10^{-2}]	$\rho_{c,b}$ [10^{14} g cm^{-3}]	$\rho_{c,pb}$ [10^{14} g cm^{-3}]	$\rho_{max,pb}$ [10^{14} g cm^{-3}]	$\beta_{ic,b}$ [10^{-2}]	$\beta_{ic,pb}$ [10^{-2}]	$M_{ic,b}$ [$M_\odot$]	$J_{ic,b}$ [10^{48} erg s]	HD [cm]	$\lvert h_{+,max}\rvert D$ [cm]	E_{GW} [$10^{-9} M_\odot c^2$]	f_{max} [Hz]	Optimal SNR @ 10 kpc
A3O6.25	6.25	0.72	3.56	2.95	2.95	10.20	9.25	0.72	4.11	190.41	389.84	49.47	770.98	102.02
A3O8.25	8.25	1.26	3.00	2.50	2.51	16.60	13.50	0.80	6.67	76.22	387.92	27.76	798.13	109.77
A3O9.25	9.25	1.58	2.67	2.26	2.27	18.60	15.62	0.84	8.17	81.96	285.48	10.51	309.12	107.21
A4O2.25*	2.25	0.24	4.24	3.49	3.49	2.40	2.06	0.60	1.22	56.28	102.99	5.63	687.20	61.89
A4O3.25	3.25	0.51	4.07	3.37	3.37	4.80	3.96	0.64	1.94	131.13	195.33	16.21	699.25	70.10
A4O4.25	4.25	0.87	3.87	3.22	3.22	7.50	6.26	0.66	2.71	208.17	283.84	35.97	708.70	76.81
A4O5.25	5.25	1.32	3.64	3.01	3.02	10.50	1.34	0.71	3.75	193.42	342.30	40.12	735.58	88.60
A4O6.25	6.25	1.88	3.33	2.79	2.79	13.40	11.02	0.74	4.88	74.85	365.52	32.99	761.24	96.00
A5O3.25	3.25	1.72	4.04	3.35	3.35	2.70	4.33	0.63	1.88	145.88	145.88	18.29	695.01	60.34
A5O3.75	3.75	2.30	3.93	3.28	3.28	4.60	5.50	0.65	2.42	188.22	251.88	28.99	704.87	71.61
A5O4.25	4.25	2.94	3.81	3.19	3.19	7.30	6.71	0.67	2.90	213.36	224.56	39.83	714.72	80.37
A5O4.75	4.75	3.70	3.70	3.10	3.11	9.50	7.94	0.70	3.37	203.52	318.81	39.00	726.86	84.63
A5O5.25	5.25	4.49	3.60	3.02	3.02	9.90	8.99	0.71	3.83	159.81	294.22	36.93	749.41	87.10

differential rotation. This is not surprising, since we showed in Sec. IV B that the GW signal amplitudes depend primarily on $\beta_{ic,b}$ both for slowly and rapidly rotating models.

To test the robustness of this conclusion, we explore the accuracy with which this analysis can extract $\beta_{ic,b}$ for injected signals that are produced using a different nuclear EOS or different $Y_e(\rho)$ parametrization. Differences in these aspects are associated with differences in the pressure, energy density, and other thermodynamic quantities. This leads to variations in the mass of the inner core at bounce ($M_{ic,b}$) and influences the dynamics of the final phase of collapse, bounce, and ring-down oscillations. The EOS dependence of GW emission from rotating core collapse was first explored by [37], while the influence of the Y_e parametrization was studied in the context of accretion-induced collapse by [39].

To evaluate the dependence of our results on the EOS, we reproduce signals for injection from the $A1$ model sequence using the Shen *et al.* [60,61] EOS in place of the Lattimer and Swesty EOS [62] used for the fiducial models listed in Tables I–II, while keeping the $Y_e(\rho)$ parametrization unchanged. We refer to this set of injections as $A1s$. To explore the dependence of the GW signals on the Y_e parametrization, we repeat the same sequence with the Lattimer and Swesty EOS but with ∼5% increased and decreased Y_e at nuclear density (sequences $A1p$ and $A1m$, respectively). The details of this parametrization are explained in the Appendix, while the characteristics of the models from these sequences are given in Table III.

In Fig. 12 we show the time evolution of the central density around the time of core bounce in models $A1O10.25$, $A1O10.25s$, $A1O10.25m$, and $A1O10.25p$. Model $A1O10.25m$ reaches the largest ρ_c at bounce and settles at the highest postbounce densities, followed by models $A1O10.25$, $A1O10.25p$, and $A1O10.25s$. Since models $A1O10.25m$ and $A1O10.25$ have smaller central Y_e than model $A1O10.25p$, the pressure in their cores is slightly lower, allowing the protoneutron star to settle at higher density. Model $A1010.25s$ (red graph) bounces and settles at a significantly lower density because the Shen *et al.* EOS [60,61] is stiffer than the Lattimer and Swesty EOS [62] at nuclear densities (see, e.g., Fig. 1 of [74]). Similar differences were observed in the simulations of Dimmelmeier *et al.* [37] who compared rotating core-collapse simulations with the $K = 180$ MeV Lattimer and Swesty EOS and Shen *et al.* EOS. In the protoneutron density regime relevant at bounce and in the early postbounce phase, the $K = 180$ MeV and $K = 220$ MeV variants of the Lattimer and Swesty EOS yield the same protoneutron star structure [7]. We refer the reader to Dimmelmeier *et al.* [37] for a more in depth discussion of the EOS dependence of rotating core collapse and the corresponding GW signals.

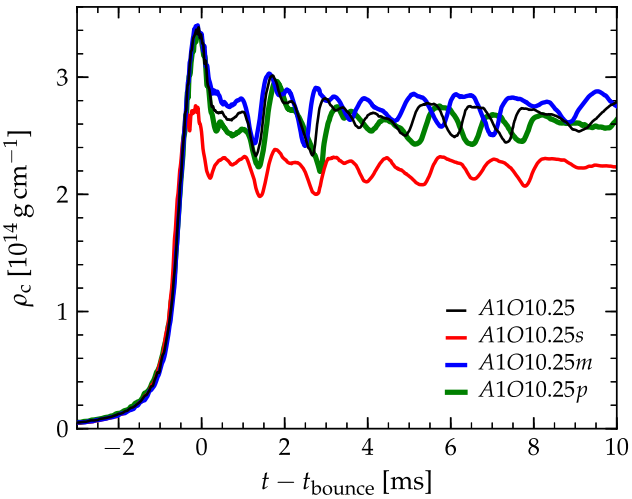

FIG. 12 (color online). Time evolution of the central density ρ_c around bounce models $A1O10.25$, $A1O10.25s$, $A1O10.25m$, and $A1O10.25p$. The black line represents ρ_c generated using the Lattimer-Swesty EOS [62] and the standard $Y_e(\rho)$ parametrization, the red graph corresponds to the model simulated with the Shen *et al.* EOS [60,61], while the blue and green graphs are simulated with ∼5% increased and decreased $Y_e(\rho)$, respectively, at nuclear densities.

Differences in the evolution of the central density are associated with differences in the overall protoneutron star dynamics, which implies differences in the GW signatures for models with different EOS and core Y_e. This is borne out by Fig. 13, which shows the GW signals of models

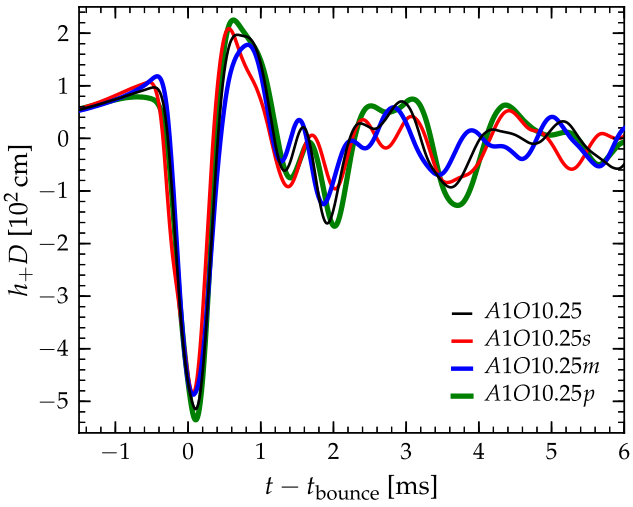

FIG. 13 (color online). GW strain h_+ rescaled by source distance D for injected waveforms $A1O10.25$, $A1O10.25s$, $A1O10.25m$, and $A1O10.25p$. The black line represents the waveform generated using the Lattimer-Swesty EOS [62] and the standard $Y_e(\rho)$ parametrization, the red graph corresponds to the model simulated with the Shen *et al.* EOS [60,61], while the blue and green graphs are simulated with ∼5% increased and decreased $Y_e(\rho)$, respectively, at nuclear densities.

$A1O10.25$, $A1O10.25s$, $A1O10.25m$, and $A1O10.25p$. Although the behavior of the GW strain appears qualitatively similar in these four cases, there are non-negligible quantitative differences stemming from the changes in the EOS and $Y_e(\rho)$ parametrization, both of which grow with increasing postbounce time.

The cyan pentagons in Fig. 11 display the measured $\beta_{\rm ic,b}$ as a function of the true $\beta_{\rm ic,b}$ for sequence $A1s$. Despite the difference between the two EOS, the matched filtering analysis measures $\beta_{\rm ic,b}$ within $\lesssim$15% of its correct value for the waveforms. The average relative deviation between measured and true $\beta_{\rm ic,b}$ for all $A1s$ models is ∼9%. Such small deviations are not surprising given the relatively weak dependence of the GW signal features on the details of the EOS found by [37]. The green stars and red triangles in Fig. 11 represent the measured $\beta_{\rm ic,b}$ as a function of true $\beta_{\rm ic,b}$ for sequences $A1m$ and $A1p$, respectively. In the case of rapid rotation ($\beta_{\rm ic,b} \gtrsim 0.05$), $\beta_{\rm ic,b}$ is extracted with $\lesssim$15% accuracy with an average deviation of ∼10%, only somewhat larger than in the case of known Y_e parametrization. Stochastic GW signal components from prompt convection explain the outliers at small $\beta_{\rm ic,b}$.

Based on these results, we conclude that our matched filter analysis can extract $\beta_{\rm ic,b}$ robustly with ∼20% accuracy for GW signals from rotating collapse, bounce, and ringdown oscillations from galactic core-collapse events. This measurement is rather robust and not very sensitive to uncertainties in inner-core Y_e and EOS.

2. Extraction of the differential rotation parameter A

The upper panel of Fig. 14 shows the quantity $\delta i = \mathrm{IDX}[A_{\rm meas.}] - \mathrm{IDX}[A_{\rm inj.}]$ as a function of $\beta_{\rm ic,b}$, where $\mathrm{IDX}[A_{\rm meas.}]$ is the integer index of the differential rotation parameter $A_{\rm meas.}$ extracted by the matched filter analysis. $\mathrm{Idx.}[A_{\rm inj.}]$ is the index of the true value of A for the injected signal (e.g., $\mathrm{Idx.}[A] = 2$ for $A = A2$). In this construction, $\delta i = 0$ ($\delta i \neq 0$) for the correct (incorrect) measurement of A. It is important to point out a caveat in measuring the degree of differential rotation using the method outlined here. The differential rotation law considered in this paper is somewhat artificial, and it is not known if the cores of massive stars obey this. We therefore remind the reader that we present the ability to measure the distribution of angular momentum in core-collapse supernova progenitors, given that they obey the rotation law given by Eq. (1).

For sequences $A1$, $A4$, and $A5$, the values of A are identified correctly for all injected signals. For sequences $A3$ ($A2$), A is determined accurately for 71% (88%) of injected waveforms. Moreover, we find that A corresponds to the next closest value in all misidentification cases. We note that misidentifications occur only for slowly rotating models. For $\beta_{\rm ic,b} \gtrsim 0.08$, A is correctly determined for all injected waveforms. More slowly rotating models emit weaker GWs, so their signal-to-noise ratio in the detector is lower, which could be a potential cause of the

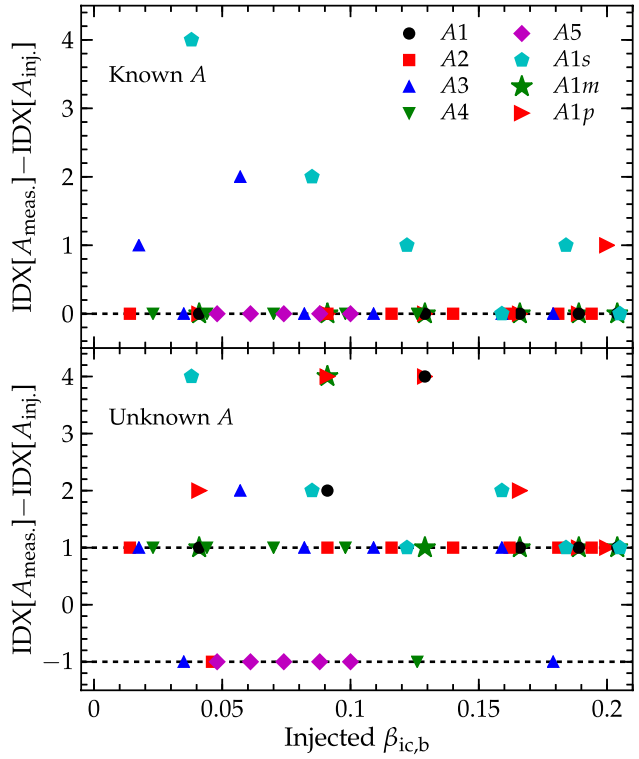

FIG. 14 (color online). $\delta i = \mathrm{IDX}[A_{\rm meas.}] - \mathrm{IDX}[A_{\rm inj.}]$ as a function of $\beta_{\rm ic,b}$. $\mathrm{IDX}[A_{\rm inj.}]$ and $\mathrm{IDX}[A_{\rm meas.}]$ denote the indices of the true and inferred values of differential rotation parameter A. As mentioned previously, $\delta i = 0$ ($\delta i \neq 0$) signify that A has been correctly (incorrectly) identified. The upper and lower panels represent the cases in which the true value of A is and is not encompassed by the template bank, respectively.

misidentification. However, tests in which we placed such models at closer distances revealed that misidentifications occur even at high signal-to-noise ratio. It is, hence, more likely that the convective component of the GW signal, which dominates in slowly rotating models, spoils the identification with the correct A. Our finding is also consistent with the notion that the degree of differential rotation plays a significant role only at rapid rotation (see Sec. IV B).

For the $A1m$ and $A1p$ signals, in which Y_e in the inner core is decreased and increased, respectively, A is inferred correctly for 100% and 83% of injections. We find that A corresponds to the next closest value in the misidentification cases.

For the $A1s$ signals, in which the Shen *et al.* [60,61] EOS is used in place of the Lattimer and Swesty EOS [62], A is inferred correctly for only two rapidly rotating models ($\simeq$33% of all models from these sequences) with $\beta_{\rm ic,b}$ of $\sim$0.16 and $\sim$0.2 (shown with cyan pentagons in Fig. 14 and denoted as $A1s$). Another $\sim$33% of models have $|\delta i| = 1$, while the remainder are measured with $|\delta i| > 1$. This suggests that, unlike $\beta_{\rm ic,b}$, A is rather sensitive to details of the nuclear EOS, and is thus more difficult to infer and features signifying different A can be confused with features imprinted due to differences in the EOS. This is supported by the correct identification of A only for rapid rotation. Rapidly rotating models reach lower maximum densities than slowly spinning ones, where differences in EOS are less pronounced than in the high density regime.

To further test the robustness of our conclusions, we use GW injections characterized by A not represented in the template bank. Here, we inject signals from model Ai, and filter the data only with templates associated with models Aj, $j \neq i$. The lower panel of Fig. 14 presents δi as a function of $\beta_{\rm ic,b}$ for this scenario. Here, $\delta i = \pm 1$ implies $A_{\rm meas.}$ is estimated to be the closest available value of A. For $A2$, $A4$, and $A5$, all injections are associated with the closest Ai. For $A3$, 87% of the injections are found with $\delta i = \pm 1$, while the remainder have $\delta i = 2$. For sequence $A1$, 67% of injections return $\delta i = \pm 1$, while the remainder return $\delta i = 2, 3$. We find that for models $A1m$, $A1p$, and $A1s$, $\delta i = \pm 1$ for 67%, 33%, and 50% of injections, respectively. Signals with EOS and $Y_{\rm e}(\rho)$ parametrization different from the fiducial ones result in a larger measurement error in the inferred value of A.

B. Bayesian model selection

We present now an alternative method to investigate the dependence of the features of the GW signal on the differential rotation parameter A and its detectability. We employ a Bayesian approach utilizing principal component analysis (PCA) [97], building upon previous work by Röver *et al.* [98] and Logue *et al.* [67].

As discussed in previous sections, GW signals from progenitors characterized by any given A are expected to exhibit some strong common features. To exploit this, we apply PCA to catalogs of waveforms characterized by a common A for each value of A. Principal component analysis isolates dominant features of waveforms into linearly independent principal components, ordered by their relevance. Mathematically, utilizing matrix C containing a given waveform catalog, one can factorize C as

$$C = U\Sigma V^T, \tag{10}$$

where U and V are matrices comprised of the eigenvectors of CC^T and C^TC, respectively, and Σ is a diagonal matrix, composed of the square roots of corresponding eigenvalues. The principal components, U, are organized according to their corresponding eigenvalues, such that the more dominant principal components (characterized by larger eigenvalues) are shifted to the first few columns of U. Approximations to waveforms in C, in addition to arbitrary waveforms, can be constructed as

$$h_i \approx \sum_j U_{ij}\epsilon_j, \tag{11}$$

where h is the desired waveform approximation, and $\vec{\epsilon}$ contains the projections of the original waveforms onto the U basis, hereafter referred to as principal component coefficients.

As in Sec. V A, we model the GW detector data, $\tilde{d}$, as containing both some core-collapse supernova GW signal $\tilde{h}(f;\vec{\lambda})$ and Gaussian noise $\tilde{n}$, colored by known one-sided PSD $S_h(f)$, where $\tilde{d}$ and λ are given by expressions (2) and (3), respectively. We consider trial templates or signals, $\tilde{h}(f;\vec{\mu})$, where

$$\vec{\mu} = \{\vec{\epsilon}, \vec{\lambda}\}, \tag{12}$$

which are reconstructed using principal components.

Our goal is to compute the evidence, $p(d|\mathcal{H})$, that the data observed contain a GW signal reconstructable from different sets of principal components, each associated with a particular degree of differential rotation. The evidence, or marginal likelihood, of the model $\mathcal{H}$ is calculated as

$$p(d|\mathcal{H}) = \int_{\vec{\mu}} p(d|\vec{\mu};\mathcal{H}) p(\vec{\mu}|\mathcal{H}) d\vec{\mu}, \tag{13}$$

where $p(\vec{\mu}|\mathcal{H})$ is the prior distribution on the parameters, given the signal model (assumed to be flat in the absence of any physical motivation to do otherwise) and $p(d|\vec{\mu};\mathcal{H})$ is the likelihood function for the data. Due to the Gaussian statistics of the noise, the likelihood function for the presence of some signal $\tilde{h}(f_i;\vec{\mu})$ can be written as

$$p(d|\vec{\mu};\mathcal{H}) = \prod_i \frac{1}{\sigma_i\sqrt{2\pi}} \exp\left(-\frac{|\tilde{d}_i - \tilde{h}(f_i;\vec{\mu})|^2}{2\sigma_i^2}\right). \tag{14}$$

Here, σ_i^2 is the variance of the noise in the ith frequency bin, related to the PSD as

$$S_h(f_i) = 2\frac{\Delta t^2}{T}\sigma_i^2, \tag{15}$$

where Δt and T are the sampling time step (the inverse of the sampling frequency) and the total observation time, respectively. To compute the evidence, we utilize an implementation of the nested sampling algorithm [99]. We perform an analysis closely linked to previous work by [67,98]. We compute the relative Bayes factor, $\log B_{i;j} = \log p(d|i) - \log p(d|j)$, between models i and j, to determine whether the evidence for model i is either greater than ($B_{i;j} > 0$) or less than ($B_{i;j} < 0$) the evidence for model j. We compare a single signal model i to the noise model via $\log B_i = \log p(d|i) - \log p(d, \text{noise})$.

Connecting this to the physical motivation of our analysis, models i and j are principal component (PC) sets constructed from waveform catalogs characterized by different values of A. We normalize the Bayes factor for the correct model B_{true} for each injected signal, to illustrate whether the correct model for A has been chosen. To do this, we compute

$$\log B_{\text{true};j} = \log B_{\text{true}} - \max[\log B_j], \tag{16}$$

where $\max[\log B_j]$ is the maximum logarithmic Bayes factor obtained for values of A other than the true one. $\log B_{\text{true};j} > 0$ ($\log B_{\text{true};j} < 0$) states that the correct model for A has (has not) been inferred. As is common in Bayesian model selection, we impose a confidence threshold η, such that $\log B_{i;j} > \eta$ states that model A_i is more likely than A_j with statistical significance. Following the conventions in Logue *et al.* [67], we set $\eta = 5$.

As in Sec. V A, we utilize simulated Gaussian noise colored by the zero-detuned high power configuration of aLIGO [94], in the context of a single, optimally oriented GW detector. We assume that the position, inclination, and polarization of the source are known, such that the antenna response functions are given by $F_+ = 1, F_\times = 0$, and place all sources at a known distance of 10 kpc. Limited by the size of the smallest waveform catalog, we use a subset of 10 PCs from each set to approximately reconstruct injected waveforms. Given this, the parameter space $\vec{\mu}$ is reduced to a ten-dimensional subset, such that $\vec{\mu} \to \vec{\epsilon}$, where $\vec{\epsilon} = \{\epsilon_1, \ldots, \epsilon_{10}\}$.

We construct PCs using the model waveforms described in Tables I and II. The injected signals are the same used for injection in Sec. V A, which are distinct from those used to generate the PCs.

Figure 15 presents the normalized $\log B_{\text{true},j}$ for all injected waveforms. Large values of $\log B_{\text{true},j}$ indicate a high degree of confidence in the chosen model for A. The dashed black line represents the detectability threshold $\log B_{\text{true},j} = 5$ discussed above. At $\beta_{\text{ic,b}} \lesssim 0.05$, most injected signals across all A have negative $\log B_{\text{true},j}$, suggesting that it is difficult to infer the correct model for A in the slow rotation limit. Tests with sources located at closer distances show that this is not a consequence of the low signal-to-noise ratio of the GW signal emitted by such models. Instead, it is most likely due to a combination of the facts that (i) the stochastic GW signal from prompt convection is comparable to or stronger than the signal from collapse, bounce, and ring down, and (ii) that there is little influence of A on the magnitude of the peaks of the GW signal at slow rotation (see Sec. IV B).

For a given $\beta_{\text{ic,b}}$, model $A1$, which is the most strongly differentially rotating, has the largest $\log B_{\text{true},j}$, suggesting that the ability to infer A with this method is greatest in extremely differentially rotating models. We also see that the magnitude of $\log B_{\text{true},j}$ tends to grow with increasing $\beta_{\text{ic,b}}$, and the correct model for A is determined for the majority of injections with $\beta_{\text{ic,b}} \gtrsim 0.08$. This is in agreement with our GW peaks analysis in Sec. IV B, where significant dependence on A is observed in the large $\beta_{\text{ic,b}}$ regime.

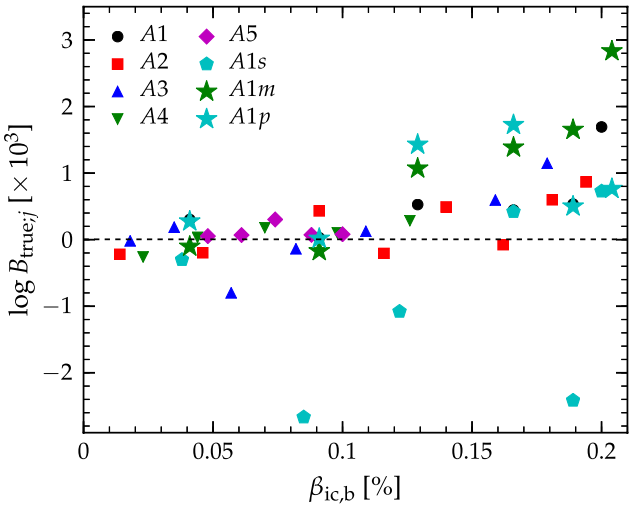

FIG. 15 (color online). $\log B_{\mathrm{true};j}$ for all injected waveforms. $\log B_{\mathrm{true};j} > 0$ and $\log B_{\mathrm{true};j} < 0$ imply correct and incorrect inference of A, respectively. Large values of $\log B_{\mathrm{true};j}$ convey that the correct model has been chosen with a high degree of confidence. The black dashed line denotes the confidence threshold $\log B_{\mathrm{true};j} = 5$ (see main text for a definition of this threshold). We see that $\log B_{\mathrm{true};j}$ increases with $\beta_{\mathrm{ic,b}}$, and, at a given $\beta_{\mathrm{ic,b}}$, A is inferred correctly with the highest confidence for injections associated with the strongest differential rotation ($A1$). In the limit of slow rotation ($\beta_{\mathrm{ic,b}} \lesssim 0.05$), the correct model for A is not determined for most injections. Incorrect A is chosen for all injections simulated with the Shen *et al.* [60,61] EOS ($A1s$), with the exception of two models characterized by extremely rapid rotation ($\beta_{\mathrm{ic,b}} \sim 0.16$).

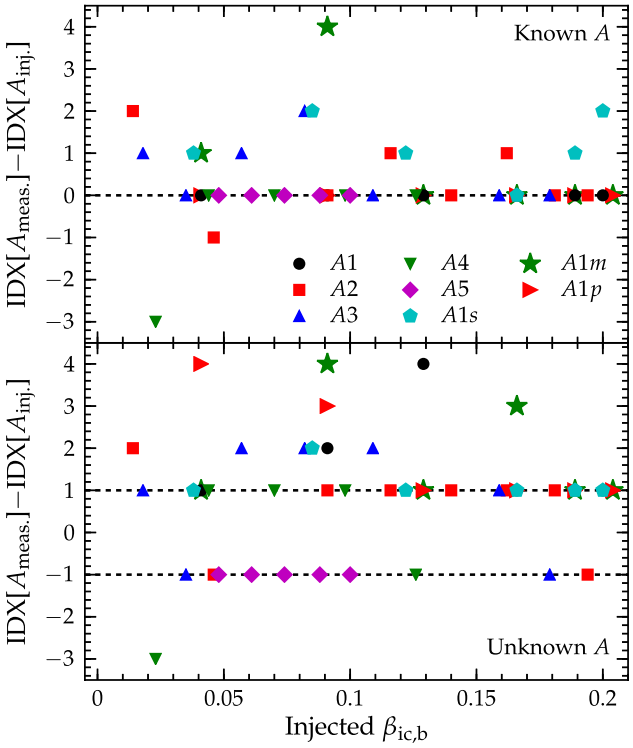

FIG. 16 (color online). The quantity $\delta i = \mathrm{Idx.}[A_{\mathrm{meas.}}] - \mathrm{Idx.}[A]$ as a function of $\beta_{\mathrm{ic,b}}$, where $\mathrm{Idx.}[A_{\mathrm{meas.}}]$ is the index of the differential rotation parameter $A_{\mathrm{meas.}}$ inferred by the model selection analysis, and $\mathrm{Idx.}[A]$ is the index of the true value of A (e.g., $\mathrm{Idx.}[A] = 2$ for $A = A2$). The upper and lower panels display results for cases in which A for all injections is known and unknown, respectively.

To test the robustness of this conclusion, we inject the waveform set $A1s$ simulated with the Shen *et al.* EOS [60,61], described in Sec. V A. We find that, in this case, the correct model for A is determined only for two models with very rapid rotation (with $\beta_{\mathrm{ic,b}}$ of $\sim$0.16 and $\sim$0.2). The maximum densities reached in these cases are relatively low, and the two EOS are not very different in this regime. In the slow rotation limit, the injected signals are strongly associated with incorrect models for A. This suggests that, if the differences between the true nuclear EOS and that used for PC construction are of the same order as the differences between the Lattimer and Swesty [62] and Shen *et al.* [60,61] EOS, then the inference of the progenitor's angular momentum distribution from the GW signal observed is significantly more difficult than if the nuclear EOS was known. This conclusion is consistent with that of the matched filter analysis presented in Sec. V A.

We also inject waveform sets $A1m$ and $A1p$, simulated with modified $Y_{\mathrm{e}}(\rho)$ parametrization, as explained in Sec. V A. For these injections (marked with large green stars and red triangles, respectively, in Fig. 15), the correct model for A is determined in the limit of fast rotation, whereas the wrong model is chosen in the slow rotation regime. In addition, we find that for models with correctly chosen A, the magnitude of $\log B_{i,j}$ is smaller than for injections from the $A1$ sequence where the $Y_{\mathrm{e}}(\rho)$ parametrization is known. This suggests that, unless Y_{e} in the inner core is known to within 5% accuracy, our ability to infer the correct model for A suffers greatly.

The upper panel of Fig. 16 shows $\delta i = \mathrm{IDX}[A_{\mathrm{meas.}}] - \mathrm{IDX}[A_{\mathrm{inj.}}]$ (as previously defined) as a function of $\beta_{\mathrm{ic,b}}$ for the injected waveforms. Here, $\mathrm{IDX}[A_{\mathrm{meas.}}]$ is the index of the differential rotation parameter $A_{\mathrm{meas.}}$ determined by Bayesian model selection, where $\log B_{\mathrm{meas,j}} > 5$ by definition. For most injections, $\delta i = 0$, signifying that the correct model for A has been inferred. We note that the fraction of injections with $\delta i = 0$ grows with increasing $\beta_{\mathrm{ic,b}}$, which is consistent with the previous conclusion that the ability to determine A is greater for rapidly rotating models. For models $A1$, $A2$, $A3$, $A4$, and $A5$, A is measured correctly in $\simeq$100%, $\simeq$50%, $\simeq$57%, $\simeq$80%, and $\simeq$100% of cases. For sequences $A1m$, $A1p$, and $A1s$, A is correctly inferred in $\simeq$67%, $\simeq$100%, and $\simeq$17% of cases, respectively. These values are consistent with those obtained from the matched filter analysis.

The lower panel of Fig. 16 shows δi as a function of $\beta_{\mathrm{ic,b}}$ for the case of injections with unknown A, for which the correct model for A is excluded from the model selection analysis. In this case, we see that the majority of injected

models have $\delta i = \pm 1$, implying identification with the closest A to that injected. Measurement of A once more improves with increasing $\beta_{\rm ic,b}$.

To conclude this section, we note that a directly comparable analysis for $\beta_{\rm ic,b}$ is not possible, since, for a given A, many parameters affect $\beta_{\rm ic,b}$, such as $\Omega_{\rm c}$, EOS, and $Y_{\rm e}(\rho)$ parametrization. However, a roughly analogous analysis could be constructed in which models describe ranges of $\beta_{\rm ic,b}$ (e.g., $0 \leq \beta_{\rm ic,b} \leq 0.05$) rather than discrete values. This blurs the line between model selection and parameter estimation, since the proposed models are just subsets of one model for $\beta_{\rm ic,b}$, rather than different models. Instead, we try to estimate some range on $\beta_{\rm ic,b}$, within which it is most likely to be. Well-posed Bayesian methods for parameter estimation typically require a continuous analytical model describing the parameter dependence of the system [99]. Such an analytic model (which could, e.g., be constructed by interpolating between discrete waveforms) is not presently available to us. Hence, we choose to postpone Bayesian parameter estimation of $\beta_{\rm ic,b}$ to future work.

VI. SUMMARY AND CONCLUSIONS

Observations of stellar surface velocities show that most massive stars rotate and some do so with velocities close to breakup (e.g., [100,101]). The internal distribution of angular momentum is, however, rather uncertain and this is true in particular for the cores of presupernova stars. Rotation can influence the collapse, bounce, and postbounce dynamics and may play a role in driving the explosion. It is thus important to understand, or, better, measure the angular momentum distribution in the core of massive stars. As we have shown in this paper, the observation of GWs from the next galactic core-collapse supernova may offer us the opportunity to do just that.

We have carried out an extensive set of axisymmetric general-relativistic simulations of rotating core collapse to study the influence of the angular momentum distribution on the GW signal of rotating collapse, bounce, and the very early postbounce ring-down phase. In total, we have simulated 124 different models, systematically probing the effects of total rotation (parametrized either by the angular momentum of the homologous inner core at bounce or by $\beta_{\rm ic,b} = T/|W|_{\rm ic,b}$) and the precollapse degree of differential rotation. We have also performed simulations with a different nuclear EOS, variations in the electron fraction of the inner core, and increased numerical resolution to test for systematic uncertainties. We have employed a single presupernova stellar model, since we have previously (in [38]) shown that for a given angular momentum distribution as a function of enclosed mass, EOS, and electron capture treatment, the universal nature of core collapse [102,103] washes out variations due to differences in precollapse progenitor structure.

Our results show that the overall dynamics of rotating core collapse is rather insensitive to the precise distribution of angular momentum within the inner core. We find that there is a simple linear mapping between the two total rotation measures $J_{\rm ic,b}$ and $\beta_{\rm ic,b}$ and the centrifugally enhanced mass of the inner core at bounce ($M_{\rm ic,b}$) throughout most of the explored parameter space. Variations in the angular momentum distribution become relevant to the detailed dynamics of collapse and bounce only in very rapidly rotating cases with $\beta_{\rm ic,b} \gtrsim 0.13$–$0.15$, which corresponds to an inner-core angular momentum at bounce of $J_{\rm ic,b} \gtrsim 5$–6×10^{48} erg s and early postbounce density-weighted average core spin periods of $\lesssim$8–10 ms. While unimportant for the overall dynamics, differential rotation does affect the structure and postbounce evolution of the protoneutron star even in more slowly spinning cores. At fixed total rotation at bounce, more differentially rotating inner cores have more centrifugally deformed (oblate) innermost regions while their overall shape is less oblate than that of their more uniformly spinning counterparts that have more centrifugal support at greater radii (and enclosed-mass coordinates).

In slowly rotating models ($\beta_{\rm ic,b} \lesssim 0.05$), the degree of precollapse differential rotation has little influence on the GW signal and there are simple linear relationships that allow one to map back from the amplitude of the pronounced and easily identifiable bounce peak $h_{1,\rm neg}$ to $J_{\rm ic,b}$ and $\beta_{\rm ic,b}$: $J_{\rm ic,b} \approx 10^{48}(h_{1,\rm neg}D/100\ {\rm cm})$ erg s and $\beta_{\rm ic,b} \approx 2.3 \times 10^{-2}(h_{1,\rm neg}D/100{\rm cm})$. For this purpose, the distance D must be known with good accuracy, which is likely for the next galactic core-collapse supernova.

The structural changes due to differential rotation have important ramifications for the GW signal in more rapidly spinning models with $\beta_{\rm ic,b} \gtrsim 0.05$–$0.08$ ($J_{\rm ic,b} \gtrsim 2$–3×10^{48} erg s), corresponding to early postbounce protoneutron star spin periods of $\lesssim$12–16 ms. More differentially rotating models yield higher global peak GW strain amplitudes at bounce and emit more energy in GWs. Total rotation and the degree of differential rotation influence the values of the first three local extrema of the GW signal, $h_{1,\rm pos}$, $h_{1,\rm neg}$, $h_{2,\rm pos}$, in a highly systematic way.

We have exploited this systematic dependence. Our results show that it is possible to extract both total rotation (both $\beta_{\rm ic,b}$ and $J_{\rm ic,b}$, since the two are simply related) and the degree of differential rotation from a previously unknown observed galactic rotating core-collapse GW signal from a source at a known distance of $D = 10$ kpc via simple cross correlation with waveforms from a numerical template GW signal bank created from our model GW signals. Since more rapidly spinning cores have a smaller contribution to their GW signals from stochastic convective motions, this works best for rapid rotation and our matched filtering analysis can measure total rotation to within $\sim$20% for a rapidly rotating

($\beta_{\rm ic,b} \gtrsim 0.08$, $J_{\rm ic,b} \gtrsim 3 \times 10^{48}$ erg s) core at $D = 10$ kpc that is optimally oriented with respect to a single GW detector. Measuring total rotation is also possible for more slowly spinning cores, though the errors may be $\gtrsim$25–35%. Figure 17 shows the $J_{\rm ic,b}$ inferred by our matched filtering analysis as a function of the true $J_{\rm ic,b}$ associated with each injected waveform. The injected waveforms are not part of the template bank used. Thus, this represents the realistic case that the exact waveform is not known.

For rapidly rotating cores ($\beta_{\rm ic,b} \gtrsim 0.08$) the differential rotation parameter A of the employed rotation law can be extracted with good precision (maximum offset of Ai in i is ± 1). We find the same result if we instead apply principal component analysis and Bayesian model selection for the five choices of differential rotation parameter $Ai, i \in [1, 5]$ that we consider in this study.

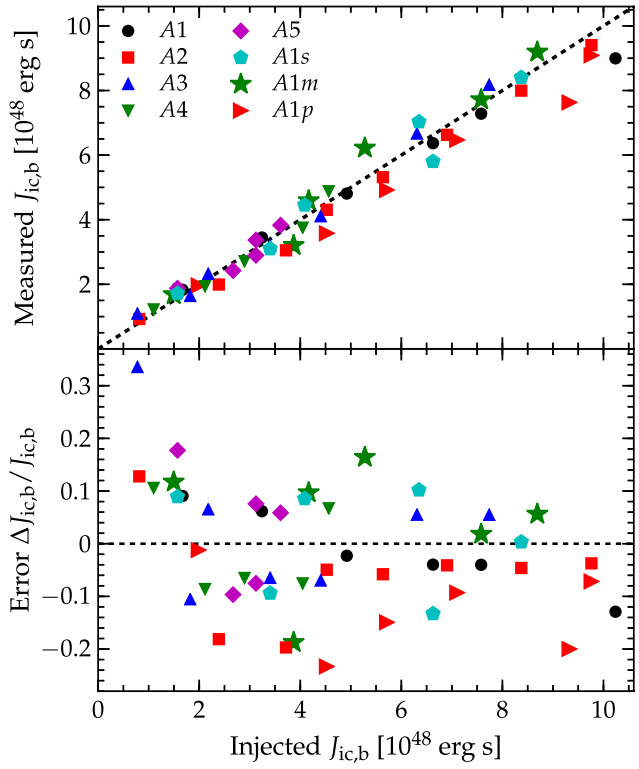

FIG. 17 (color online). Results of our matched filtering analysis (Sec. V A) for the angular momentum of the inner core at bounce ($J_{\rm ic,b}$). Top panel: Extracted $J_{\rm ic,b}$ as a function of $J_{\rm ic,b}$ corresponding to the injected waveform. Bottom panel: relative measurement error. This analysis assumes optimal source-detector orientation and a source distance of 10 kpc. The different symbols correspond to models with different degree of differential rotation as given by the legend. The $A1s$ models are $A1$ models, but evolved with the Shen *et al.* EOS [60,61], and the $A1m$ ($A1p$) models used a $Y_e(\rho)$ parametrization during collapse that was reduced (increased) by 5% near nuclear density compared to the fiducial one. Our results show that—in the optimal case considered here—one can measure the angular momentum of the inner core at bounce with ~20–30% accuracy for a rapidly spinning galactic core-collapse supernova.

While our simulations are numerically well converged, our tests reveal important systematic uncertainties associated with the nuclear EOS and the electron fraction Y_e in the inner core at bounce. We find that a $\pm 5\%$ variation of Y_e or a change of the EOS from Lattimer and Swesty with $K = 220$ MeV [62] to the Shen *et al.* EOS [60,61] can spoil the accuracy with which we can extract total and differential rotation.

The EOS dependence of our results underlines the need for improved nuclear EOS tables that take into account all new experimental, observational, and theoretical EOS constraints [104]. Future simulations of rotating core collapse should also consider a broader range of nuclear EOS models (e.g., [105–107]) to further explore the sensitivity of the GW signal to the nuclear EOS.

Addressing uncertainties in the Y_e of the inner core will ultimately require full neutrino radiation-hydrodynamics simulations with up-to-date electron capture rates for heavy nuclei (e.g., [108]), full velocity dependence, and inelastic neutrino-electron scattering, which all have an effect on the Y_e in the inner core (e.g., [109]). Such simulations, while computationally extremely intense, are possible now, for example, with the radiation-hydrodynamic variant of the CoCoNuT code developed by B. Müller [110].

In this study, we have broken entirely new ground by combining precision computational waveform modeling with methods of GW astronomy. We have given the proof of principle that information on both total and differential rotation can be extracted, or at least constrained, from the GW signal of the next galactic core-collapse event. Future work must address our study's many deficiencies. The most important of these may be the following: (i) Although axisymmetry is an excellent approximation for collapse, bounce, and ring-down oscillations for rotating axisymmetric progenitors, the subsequent postbounce evolution (not considered in this work) is likely to exhibit nonaxisymmetric features in the GW signal [40–42]. Moreover, Kuroda *et al.* have argued that nonaxisymmetric perturbations in the inner core may alter the bounce and postbounce gravitational wave signal. It is presently unclear if such perturbations are present in the core, but they are likely to be present in the shell burning layers surrounding the core [11,111], which are irrelevant for the GW signals studied here. (ii) We considered only a single rotation law, but realistic cores of massive stars do not necessarily follow it. (iii) We assumed optimal source-detector alignment and only a single detector with Gaussian noise. A real core-collapse event is unlikely to be optimally aligned, but a network of second-generation detectors can mitigate reduced signal strength due to misalignment. (iv) We assumed the distance to the source to be known precisely. For a real core-collapse event, the distance is unlikely to be known exactly. (v) Our treatment of electron capture during

collapse relies on a single-parameter density fit of $Y_e(\rho)$ from spherically symmetric radiation-hydrodynamics simulations. Rapid rotation may lead to significant deviations from such simple fits in full two-dimensional radiation-hydrodynamics simulations and this could have a significant quantitative effect on the predicted GW signals.

ACKNOWLEDGMENTS

We thank P. Cerda-Duran, S. Couch, J. Clark, S. de Mink, B. Engels, R. Haas, I. S. Heng, H. Klion, J. Logue, P. Mösta, B. Müller, J. Novak, E. O'Connor, U. C. T. Gamma, C. Reisswig, L. Roberts, and A. Weinstein for helpful discussions. This work is supported by the National Science Foundation under Grants No. PHY-1151197, No. AST-1212170, No. OCI-0905046, and No. PHY-1068881, by the Sherman Fairchild Foundation, and by the Alfred P. Sloan Foundation. Results presented in this article were obtained through computations on the Caltech computer cluster "Zwicky" (NSF MRI Grant No. PHY-0960291), on the NSF XSEDE network under Grant No. TG-PHY100033, on machines of the Louisiana Optical Network Initiative, and at the National Energy Research Scientific Computing Center (NERSC), which is supported by the Office of Science of the U.S. Department of Energy under Award No. DE-AC02-05CH11231.

APPENDIX: $Y_e(\rho)$ PARAMETRIZED DELEPTONIZATION SCHEME

Following [77], we use the following fitting function to model the functional dependence of Y_e on ρ:

$$Y_e = \frac{1}{2}(Y_{e,1} + Y_{e,1}) + \frac{x}{2}(Y_{e,1} - Y_{e,1}) + Y_{e,c}[1 - |x| + 4|x|(|x| - 1/2)(|x| - 1)], \quad \text{(A1)}$$

where

$$x = \max\left[-1, \min\left(1, \frac{2\log\rho - \log\rho_2 - \log\rho_1}{\log\rho_2 - \log\rho_1}\right)\right] \quad \text{(A2)}$$

and $\rho_1 = 10^7\ \mathrm{g\,cm^{-3}}$, $\rho_2 = 10^{13}\ \mathrm{g\,cm^{-3}}$, $Y_{e,1} = 0.5$, $Y_{e,2} = 0.29$, and $Y_{e,c} = 0.035$. When density ρ is above ρ_2, we make the following correction to Y_e:

$$Y_e = Y_e(\rho_2) + \frac{\log\rho - \log\rho_2}{\log\rho_{cor} - \log\rho_2}[Y_{e,cor} - Y_e(\rho_2)], \quad \text{(A3)}$$

where $\rho_{cor} = 2.55 \times 10^{14}\ \mathrm{g\,cm^{-3}}$ and $Y_{e,cor}$ is chosen to be 0.2717 for our fiducial $Y_e(\rho)$ parametrization. In our 5% reduced (increased) $Y_e(\rho)$ parametrization, we use a 5% smaller (larger) value of $Y_{e,cor}$.

[1] H. A. Bethe, Rev. Mod. Phys. **62**, 801 (1990).
[2] H. A. Bethe and J. R. Wilson, Astrophys. J. **295**, 14 (1985).
[3] H.-T. Janka, F. Hanke, L. Hüdepohl, A. Marek, B. Müller, and M. Obergaulinger, Prog. Theor. Exp. Phys. **2012**, 1A309 (2012).
[4] A. Burrows, Rev. Mod. Phys. **85**, 245 (2013).
[5] J. M. Blondin, A. Mezzacappa, and C. DeMarino, Astrophys. J. **584**, 971 (2003).
[6] S. W. Bruenn, A. Mezzacappa, W. R. Hix, E. J. Lentz, O. E. Bronson Messer, E. J. Lingerfelt, J. M. Blondin, E. Endeve, P. Marronetti, and K. N. Yakunin, Astrophys. J. Lett. **767**, L6 (2013).
[7] B. Müller, H.-T. Janka, and A. Marek, Astrophys. J. **756**, 84 (2012).
[8] B. Müller, H.-T. Janka, and A. Heger, Astrophys. J. **761**, 72 (2012).
[9] F. Hanke, B. Müller, A. Wongwathanarat, A. Marek, and H.-T. Janka, Astrophys. J. **770**, 66 (2013).
[10] T. Takiwaki, K. Kotake, and Y. Suwa, Astrophys. J. **786**, 83 (2014).
[11] S. M. Couch and C. D. Ott, Astrophys. J. Lett. **778**, L7 (2013).
[12] M. R. Drout, A. M. Soderberg, A. Gal-Yam, S. B. Cenko, D. B. Fox, D. C. Leonard, D. J. Sand, D.-S. Moon, I. Arcavi, and Y. Green, Astrophys. J. **741**, 97 (2011).
[13] N. Smith, W. Li, A. V. Filippenko, and R. Chornock, Mon. Not. R. Astron. Soc. **412**, 1522 (2011).
[14] M. T. Botticella, C. Trundle, A. Pastorello, S. Rodney, A. Rest, S. Gezari, S. J. Smartt, G. Narayan, M. E. Huber, J. L. Tonry *et al.*, Astrophys. J. Lett. **717**, L52 (2010).
[15] N. Smith, S. B. Cenko, N. Butler, J. S. Bloom, M. M. Kasliwal, A. Horesh, S. R. Kulkarni, N. M. Law, P. E. Nugent, E. O. Ofek *et al.*, Mon. Not. R. Astron. Soc. **420**, 1135 (2012).
[16] M. Modjaz, Astron. Nachr. **332**, 434 (2011).
[17] J. Hjorth and J. S. Bloom, in *Gamma-Ray Bursts*, edited by C. Kouveliotou, R. A. M. J. Wijers, and S. E. Woosley (Cambridge University Press, Cambridge, 2011).
[18] G. S. Bisnovatyi-Kogan, Astron. Zh. **47**, 813 (1970).
[19] J. M. LeBlanc and J. R. Wilson, Astrophys. J. **161**, 541 (1970).
[20] J. C. Wheeler, I. Yi, P. Höflich, and L. Wang, Astrophys. J. **537**, 810 (2000).
[21] J. C. Wheeler, D. L. Meier, and J. R. Wilson, Astrophys. J. **568**, 807 (2002).
[22] A. Burrows, L. Dessart, E. Livne, C. D. Ott, and J. Murphy, Astrophys. J. **664**, 416 (2007).
[23] S. E. Woosley and J. S. Bloom, Annu. Rev. Astron. Astrophys. **44**, 507 (2006).

[24] B. D. Metzger, D. Giannios, T. A. Thompson, N. Bucciantini, and E. Quataert, Mon. Not. R. Astron. Soc. **413**, 2031 (2011).

[25] A. Heger, S. E. Woosley, and H. C. Spruit, Astrophys. J. **626**, 350 (2005).

[26] C. D. Ott, A. Burrows, T. A. Thompson, E. Livne, and R. Walder, Astrophys. J. Suppl. Ser. **164**, 130 (2006).

[27] S. E. Woosley and A. Heger, Astrophys. J. **637**, 914 (2006).

[28] S.-C. Yoon, N. Langer, and C. Norman, Astron. Astrophys. **460**, 199 (2006).

[29] S. E. de Mink, N. Langer, R. G. Izzard, H. Sana, and A. de Koter, Astrophys. J. **764**, 166 (2013).

[30] L. Dessart, E. O'Connor, and C. D. Ott, Astrophys. J. **754**, 76 (2012).

[31] S. A. Balbus and J. F. Hawley, Astrophys. J. **376**, 214 (1991).

[32] M. Obergaulinger, P. Cerdá-Durán, E. Müller, and M. A. Aloy, Astron. Astrophys. **498**, 241 (2009).

[33] S. Akiyama, J. C. Wheeler, D. L. Meier, and I. Lichtenstadt, Astrophys. J. **584**, 954 (2003).

[34] T. A. Thompson, E. Quataert, and A. Burrows, Astrophys. J. **620**, 861 (2005).

[35] T. K. Suzuki, K. Sumiyoshi, and S. Yamada, Astrophys. J. **678**, 1200 (2008).

[36] C. Fryer and K. C. B. New, Living Rev. Relativity **14**, 1 (2011).

[37] H. Dimmelmeier, C. D. Ott, A. Marek, and H.-T. Janka, Phys. Rev. D **78**, 064056 (2008).

[38] C. D. Ott, E. Abdikamalov, E. O'Connor, C. Reisswig, R. Haas, P. Kalmus, S. Drasco, A. Burrows, and E. Schnetter, Phys. Rev. D **86**, 024026 (2012).

[39] E. B. Abdikamalov, C. D. Ott, L. Rezzolla, L. Dessart, H. Dimmelmeier, A. Marek, and H. Janka, Phys. Rev. D **81**, 044012 (2010).

[40] C. D. Ott, H. Dimmelmeier, A. Marek, H.-T. Janka, I. Hawke, B. Zink, and E. Schnetter, Phys. Rev. Lett. **98**, 261101 (2007).

[41] S. Scheidegger, R. Käppeli, S. C. Whitehouse, T. Fischer, and M. Liebendörfer, Astron. Astrophys. **514**, A51 (2010).

[42] T. Kuroda, T. Takiwaki, and K. Kotake, Phys. Rev. D **89**, 044011 (2014).

[43] K. Kotake, C.R. Phys. **14**, 318 (2013).

[44] N. Andersson, V. Ferrari, D. I. Jones, K. D. Kokkotas, B. Krishnan, J. S. Read, L. Rezzolla, and B. Zink, Gen. Relativ. Gravit. **43**, 409 (2011).

[45] E. Müller, Astron. Astrophys. **114**, 53 (1982).

[46] R. Mönchmeyer, G. Schäfer, E. Müller, and R. Kates, Astron. Astrophys. **246**, 417 (1991).

[47] S. Yamada and K. Sato, Astrophys. J. **450**, 245 (1995).

[48] T. Zwerger and E. Müller, Astron. Astrophys. **320**, 209 (1997).

[49] K. Kotake, S. Yamada, and K. Sato, Phys. Rev. D **68**, 044023 (2003).

[50] H. Dimmelmeier, J. A. Font, and E. Müller, Astron. Astrophys. **393**, 523 (2002).

[51] M. Shibata and Y. Sekiguchi, Phys. Rev. D **69**, 084024 (2004).

[52] C. D. Ott, A. Burrows, E. Livne, and R. Walder, Astrophys. J. **600**, 834 (2004).

[53] C. D. Ott, H. Dimmelmeier, A. Marek, H.-T. Janka, B. Zink, I. Hawke, and E. Schnetter, Classical Quantum Gravity **24**, S139 (2007).

[54] H. Dimmelmeier, C. D. Ott, H.-T. Janka, A. Marek, and E. Müller, Phys. Rev. Lett. **98**, 251101 (2007).

[55] T. Takiwaki and K. Kotake, Astrophys. J. **743**, 30 (2011).

[56] K. Kotake, S. Yamada, K. Sato, K. Sumiyoshi, H. Ono, and H. Suzuki, Phys. Rev. D **69**, 124004 (2004).

[57] M. Obergaulinger, M. A. Aloy, and E. Müller, Astron. Astrophys. **450**, 1107 (2006).

[58] M. Obergaulinger, M. A. Aloy, H. Dimmelmeier, and E. Müller, Astron. Astrophys. **457**, 209 (2006).

[59] M. Shibata, Y. T. Liu, S. L. Shapiro, and B. C. Stephens, Phys. Rev. D **74**, 104026 (2006).

[60] H. Shen, H. Toki, K. Oyamatsu, and K. Sumiyoshi, Nucl. Phys. **A637**, 435 (1998).

[61] H. Shen, H. Toki, K. Oyamatsu, and K. Sumiyoshi, Astrophys. J. Suppl. Ser. **197**, 20 (2011).

[62] J. M. Lattimer and F. D. Swesty, Nucl. Phys. **A535**, 331 (1991).

[63] H. Dimmelmeier, J. A. Font, and E. Müller, Astron. Astrophys. **388**, 917 (2002).

[64] H. Dimmelmeier, J. Novak, J. A. Font, J. M. Ibáñez, and E. Müller, Phys. Rev. D **71**, 064023 (2005).

[65] M. Liebendörfer, M. Rampp, H.-T. Janka, and A. Mezzacappa, Astrophys. J. **620**, 840 (2005).

[66] S. E. Woosley and A. Heger, Phys. Rep. **442**, 269 (2007).

[67] J. Logue, C. D. Ott, I. S. Heng, P. Kalmus, and J. Scargill, Phys. Rev. D **86**, 044023 (2012).

[68] G. M. Harry (LIGO Scientific Collaboration), Classical Quantum Gravity **27**, 084006 (2010).

[69] P. Cerdá-Durán, G. Faye, H. Dimmelmeier, J. A. Font, J. M. Ibáñez, E. Müller, and G. Schäfer, Astron. Astrophys. **439**, 1033 (2005).

[70] C. D. Ott, Ph. D. thesis, Universität Potsdam, 2007, http://nbn-resolving.de/urn/resolver.pl?urn=urn:nbn:de:kobv:517-opus-12986.

[71] J. A. Font, Living Rev. Relativity **11**, 7 (2008).

[72] P. Colella and P. R. Woodward, J. Comput. Phys. **54**, 174 (1984).

[73] B. Einfeldt, in *Proceedings of the Sixteenth International Symposium, Aachen, Germany, 1987* (VCH Verlag, Weinheim, 1988), p. 671.

[74] E. O'Connor and C. D. Ott, Classical Quantum Gravity **27**, 114103 (2010).

[75] A Community Portal for Stellar Collapse, Core-Collapse Supernova, and GRB Simulations, http://www.stellarcollapse.org.

[76] E. O'Connor and C. D. Ott, Astrophys. J. **730**, 70 (2011).

[77] M. Liebendörfer, Astrophys. J. **633**, 1042 (2005).

[78] C. D. Ott, E. Abdikamalov, P. Mösta, R. Haas, S. Drasco, E. P. O'Connor, C. Reisswig, C. A. Meakin, and E. Schnetter, Astrophys. J. **768**, 115 (2013).

[79] S. M. Couch and E. P. O'Connor, Astrophys. J. **785**, 123 (2014).

[80] C. Reisswig, C. D. Ott, U. Sperhake, and E. Schnetter, Phys. Rev. D **83**, 064008 (2011).

[81] A. Heger, N. Langer, and S. E. Woosley, Astrophys. J. **528**, 368 (2000).

[82] H. C. Spruit, Astron. Astrophys. **381**, 923 (2002).

[83] N. Langer, Annu. Rev. Astron. Astrophys. **50**, 107 (2012).
[84] J. L. Friedman, L. Parker, and J. R. Ipser, Astrophys. J. **304**, 115 (1986).
[85] J. E. Tohline, Astrophys. J. **285**, 721 (1984).
[86] L. S. Shapiro and S. A. Teukolsky, *Black Holes, White Dwarfs, and Neutron Stars* (John Wiley & Sons, New York, 1983).
[87] K. Hayama, S. Desai, K. Kotake, S. D. Mohanty, M. Rakhmanov, T. Summerscales, and S. Yoshida, Classical Quantum Gravity **25**, 184022 (2008).
[88] C. W. Helstrom, *Statistical Theory of Signal Detection*, 2nd ed. (Pergamon Press, New York, 1968).
[89] C. D. Ott, Classical Quantum Gravity **26**, 063001 (2009).
[90] K. Kotake, W. Iwakami, N. Ohnishi, and S. Yamada, Astrophys. J. Lett. **697**, L133 (2009).
[91] C. D. Ott, A. Burrows, L. Dessart, and E. Livne, Astrophys. J. **685**, 1069 (2008).
[92] C. W. Misner, K. S. Thorne, and J. A. Wheeler, *Gravitation* (W. H. Freeman and Co., San Francisco, 1973).
[93] G. González and (LIGO Science Collaboration), Classical Quantum Gravity **21**, S691 (2004).
[94] D. Shoemaker (LIGO Scientific Collaboration), Report No. LIGO-T0900288-v3, 2010, https://dcc.ligo.org/cgi-bin/DocDB/ShowDocument?docid=t0900288.
[95] P. Ajith, M. Boyle, D. A. Brown, S. Fairhurst, M. Hannam, I. Hinder, S. Husa, B. Krishnan, R. A. Mercer, F. Ohme *et al.*, arXiv:0709.0093v3.
[96] C. Cutler, T. A. Apostolatos, L. Bildsten, L. S. Finn, E. E. Flanagan, D. Kennefick, D. M. Markovic, A. Ori, E. Poisson, and G. J. Sussman, Phys. Rev. Lett. **70**, 2984 (1993).
[97] K. V. Mardia, J. T. Kent, and J. M. Bibby, *Multivariate Analysis* (Academic Press, New York, 1980).
[98] C. Röver, M. Bizouard, N. Christensen, H. Dimmelmeier, I. S. Heng, and R. Meyer, Phys. Rev. D **80**, 102004 (2009).
[99] J. Skilling, AIP Conf. Proc. **735**, 395 (2004).
[100] O. H. Ramírez-Agudelo, S. Simón-Díaz, H. Sana, A. de Koter, C. Sabín-Sanjulían, S. E. de Mink, P. L. Dufton, G. Gräfener, C. J. Evans, A. Herrero *et al.*, arXiv:1309.2929 [Astron. Astrophys. (to be published)].
[101] W. Huang, D. R. Gies, and M. V. McSwain, Astrophys. J. **722**, 605 (2010).
[102] P. Goldreich and S. V. Weber, Astrophys. J. **238**, 991 (1980).
[103] A. Yahil, Astrophys. J. **265**, 1047 (1983).
[104] J. M. Lattimer and Y. Lim, Astrophys. J. **771**, 51 (2013).
[105] G. Shen, C. J. Horowitz, and S. Teige, Phys. Rev. C **83**, 035802 (2011).
[106] G. Shen, C. J. Horowitz, and E. O'Connor, Phys. Rev. C **83**, 065808 (2011).
[107] A. W. Steiner, M. Hempel, and T. Fischer, Astrophys. J. **774**, 17 (2013).
[108] A. Juodagalvis, K. Langanke, W. R. Hix, G. Martínez-Pinedo, and J. M. Sampaio, Nucl. Phys. **A848**, 454 (2010).
[109] E. J. Lentz, A. Mezzacappa, O. E. Bronson Messer, M. Liebendörfer, W. R. Hix, and S. W. Bruenn, Astrophys. J. **747**, 73 (2012).
[110] B. Müller, Ph. D. thesis, Technische Universität München, 2009.
[111] W. D. Arnett and C. Meakin, Astrophys. J. **733**, 78 (2011).